INTERNATIONAL JOURNAL FOR NUMERICAL METHODS IN FLUIDS, VOL. 23, 1043–1072 (1996)

INTERNAL LEE WAVES AND TURBULENCE MIXING OVER AN ISOLATED SEAMOUNT: RESULTS FROM TURBULENCE ENERGY MODELS

JIUXING XING AND ALAN M. DAVIES

Proudman Oceanographic Laboratory, Bidston Observatory, Birkenhead, Merseyside L43 7RA, U.K.

SUMMARY

A three-dimensional, primitive equation, baroclinic numerical model incorporating a range of turbulence energy submodels is used to study the generation of internal lee waves over an isolated seamount. Attention is given to the turbulence mixing enhanced by the internal lee waves. The results show that regions of strong turbulence energy appear over the lee side of the seamount associated with the production of the lee waves. The computed vertical eddy viscosity and diffusivity using turbulence models can be as large as 1 m^2s^{-1}.

A comparison of the magnitude and spatial distribution of the internal lee waves does not reveal any major differences in results computed using different turbulence energy models or mixing determined from a Richardson number formulation. However, the magnitude of the vertical mixing is sensitive to the form of turbulence energy submodel. Also, a study of the relevant importance of the various terms in the turbulence energy equation shows that the term representing the advection of turbulence needs to be retained in order to accurately reproduce the mixing produced by the internal lee waves. Calculations using a range of seamount profiles show that the magnitude of near-bed turbulence is sensitive to the shape of the seamount.

The magnitude and spatial distribution of the lee waves and associated flow field are affected by the parametrization of horizontal diffusion, with significant differences between the use of Laplacian and biharmonic forms of horizontal diffusion. The application of biharmonic horizontal diffusion is recommended.

KEY WORDS: lee-waves; seamount; turbulence-energy; mixing

1. INTRODUCTION

In recent years, three-dimensional shallow sea modelling has concentrated upon finer grid, limited area models[1] where bed topographic features can be accurately resolved within the model and their effects upon bed friction[2] and circulation examined in detail. Although in these models the subgrid-scale vertical mixing has in many cases been parametrized using the eddy viscosity coefficient,[3] there is now a trend to use higher-turbulence schemes[4] to parametrize the turbulent processes associated with topographic features.

In ocean circulation studies the majority of models have used large-area coarse grids with constant mixing coefficients. However, in recent years there has been increasing evidence that topographic features such as seamounts and the lee waves and mixing associated with them have an important effect upon the large-scale circulation. As limited area ocean circulation models with fine grids are developed, there is a need to examine methods to accurately model the flow and in particular the mixing associated with topographic features and the internal waves induced by them: the topic of this paper.

CCC 0271–2091/96/101043–30

Received January 1996

Internal lee waves are generated when a stably stratified fluid passes an obstacle.[5] There has been significant research on internal lee waves in the atmosphere,[6] generated by the stratified atmospheric flow over mountains, and reviews can be found in References 7 and 8. In the ocean, however, there has been less attention given to the possibility of internal lee waves over the bottom topography, such as a seamount or shelf edge, although internal waves and internal tides have been studied for many years.[9–14]

The scale difference between oceanic flow and atmospheric flow means that the earth's rotation plays a more important role in the oceanic flow over a seamount than in the atmospheric flow over a mountain. In the case of internal lee waves generated in the atmospheric flow over mountains, the scale is often not large enough for rotation effects to be important[5] (i.e. non-rotating wave regime). If the hydrostatic approximation is applicable and rotational effects are neglected (i.e. hydrostatic non-rotating regime), waves are found only above the mountain, because the group velocity propagation is vertical. In the ocean, however, the hydrostatic assumption is almost always valid, so the horizontal propagation of internal waves requires the effect of the earth's rotation. In this situation, internal lee waves can only be generated when the imposed background Froude number (defined by $F = U_i/NH_0$, where U_i is the imposed mean velocity, N is the buoyancy frequency and H_0 is the water depth) is above a critical value.

Chapman and Haidvogel[15] (hereinafter CH93) have studied the possibility of the generation of internal lee waves in an oceanic environment. Using a primitive equation numerical model, they studied the generation of internal lee waves in a steady, rotating, uniformly stratified flow past an isolated seamount. In many cases that they examined, the imposed background Froude number was not large enough to generate mode 1 internal lee waves. However, they still found large-amplitude mode 1 internal lee waves which were trapped over the flank of the seamount where non-linear advection of momentum led to large local acceleration of the flow and therefore increased the local Froude number. According to CH93, the decay of the internal waves is due to two factors: the deceleration of the flow downstream of the seamount and subgrid-scale mixing. In particular, the deceleration of the mean flow reduces the internal wave wavelength and the resulting small-wavelength wave can be more rapidly dissipated by viscous effects.

The modelling approach of CH93 was based upon using an expansion in terms of functions in the vertical and therefore could not take account of turbulent mixing processes which are significant in the lee of seamounts. Their model also had a rigid lid. Here, following the earlier work of CH93, we study internal lee waves over an isolated seamount with a view to examining the turbulence mixing produced by seamount-generated lee waves. Regions of enhanced mixing in the ocean may be important in determining the extent to which the ocean mixes in general, in that oceanic mixing is thought to occur locally in regions of sloping topography and then spread into the ocean interior (a recent review of oceanic mixing is given in Reference 16). Intensive local mixing regions are clearly important from a biological point of view, in that they can increase local nutrients.[17] Also, a detailed knowledge of regions of intense mixing is important for acoustic propagation problems.[18]

In this paper we develop a three-dimensional, primitive equation, free surface model in transport form. The transport form of the equation is preferable in regions of rapidly changing topography, in that the product of terms such as velocity and water depth in such areas is a more gradually changing function than velocity alone and this improves the accuracy of the finite difference approach. The method of solution in the vertical involves a finite difference grid rather than the functional approach used in CH93. The advantage of using the finite difference method is that the model can readily incorporate a range of turbulence energy closure methods to compute the eddy viscosity and eddy diffusivity. Hence the turbulent mixing associated with the seamount can be studied using a range of turbulence closure methods and the importance of the various terms in the turbulence energy equations assessed. Also, by comparing solutions using the finite difference method with those computed by CH93 using a functional approach, the accuracy of the finite difference method can be determined.

The range of turbulence closure schemes applied here covers the main approaches used in oceanographic modelling. The computationally most intensive model uses a prognostic equation for both turbulence and mixing length, namely the closure of Mellor and Yamada.[19] This closure can be simplified and hence the computation reduced by using one prognostic equation for turbulence energy and an algebraic mixing length.[20] The simplest turbulence approach, and the one commonly employed in oceanography, is to use a Richardson-number-dependent eddy viscosity and diffusivity.[21]

By using a range of turbulence submodels, it is possible to examine how the intensity of mixing depends upon the choice of model and under what conditions simpler models can yield results comparable with more complex models. Also, a detailed comparison of the importance of the various terms in the turbulence energy equations is considered in order to determine the major processes controlling the magnitude of mixing. The sensitivity of the model results to different formulations of horizontal diffusion (biharmonic form and Laplacian form) and chosen horizontal diffusion coefficients, as well as different seamount profiles, is also investigated.

The mathematical formulation of the numerical model and the parameters used in the numerical calculations are presented in the next section. Section 3 deals with the results from model experiments concentrating on internal lee waves and wave-enhanced turbulence mixing as well as the bottom flow structure over an isolated seamount with varying seamount height and slope. The last section of the paper contains concluding remarks.

2. NUMERICAL MODEL AND PARAMETERS USED IN THE CALCULATIONS

2.1. *Model equations*

A three-dimensional, free surface, primitive equation model is used in this study. The model is based on previous work of Davies and Jones[22] and Xing and Davies[23,24] and uses a topography-following co-ordinate $\sigma = (\zeta + z)/H$. The model equations, with conventional Boussinesq and hydrostatic approximations, in transport form using σ-co-ordinates in the vertical are given by

$$\frac{\partial Hu}{\partial t} + \nabla \cdot (Hu\mathbf{V}) + \frac{\partial Hu\omega}{\partial \sigma} - fHv = -gH\frac{\partial \zeta}{\partial x} + BPF_x + \frac{1}{H^2}\frac{\partial}{\partial \sigma}\left(K_\mathrm{m}\frac{\partial Hu}{\partial \sigma}\right) + HF_u, \tag{1}$$

$$\frac{\partial Hv}{\partial t} + \nabla \cdot (Hv\mathbf{V}) + \frac{\partial Hv\omega}{\partial \sigma} + fHu = -gH\frac{\partial \zeta}{\partial y} + BPF_y + \frac{1}{H^2}\frac{\partial}{\partial \sigma}\left(K_\mathrm{m}\frac{\partial Hv}{\partial \sigma}\right) + HF_v, \tag{2}$$

$$\frac{\partial \zeta}{\partial t} + \nabla \cdot \left(\int_{-1}^{0} (H\mathbf{V})\,\mathrm{d}\sigma\right) = 0, \tag{3}$$

$$\frac{\partial HT}{\partial t} + \nabla \cdot (HT\mathbf{V}) + \frac{\partial HT\omega}{\partial \sigma} = \frac{1}{H^2}\frac{\partial}{\partial \sigma}\left(K_\mathrm{h}\frac{\partial HT}{\partial \sigma}\right) + HF_T, \tag{4}$$

$$\frac{\partial P}{\partial \sigma} = -\rho g H, \tag{5}$$

$$\rho = \rho_0[1 - \alpha(T - T_0)]. \tag{6}$$

Here $\mathbf{V} = (u, v)$ and (u, v, ω) are the velocity components corresponding to the co-ordinates (x, y, σ); ρ is the density; T is the temperature; α is the thermal expansion coefficient; T_0 and ρ_0 are the reference temperature and density; H is the total water depth given by $H = h + \zeta$; ζ is the elevation of the sea surface above the undisturbed level; h is the depth below the undisturbed level; z is the vertical co-ordinate increasing vertically upwards, with $z = \zeta$ the free surface and $z = -h$ the sea bed; f is the Coriolis parameter; g is the gravitational acceleration; t is the time; K_m and K_h are the vertical eddy viscosity and diffusivity coefficients; F_u, F_v and F_T are the horizontal diffusion terms for momentum and temperature; P is the pressure field; BPF_x and BPF_y are the baroclinic pressure force terms given by

$$BPF_x = -\frac{H\partial P_{b0}}{\rho_0 \partial x}\bigg|_z - \frac{H}{\rho_0}\left(\frac{\partial(P_b - P_{b0})}{\partial x} + \frac{\sigma}{H}\frac{\partial(P_b - P_{b0})}{\partial\sigma}\frac{\partial H}{\partial x} + \frac{\partial(P_b - P_{b0})}{H\partial\sigma}\frac{\partial\zeta}{\partial x}\right), \tag{7}$$

$$BPF_y = -\frac{H\partial P_{b0}}{\rho_0 \partial y}\bigg|_z - \frac{H}{\rho_0}\left(\frac{\partial(P_b - P_{b0})}{\partial y} + \frac{\sigma}{H}\frac{\partial(P_b - P_{b0})}{\partial\sigma}\frac{\partial H}{\partial y} + \frac{\partial(P_b - P_{b0})}{H\partial\sigma}\frac{\partial\zeta}{\partial y}\right), \tag{8}$$

where P_{b0} is a reference baroclinic pressure or the initial baroclinic pressure field. The first terms on the right of (7) and (8) are the pressure forces calculated on the z-co-ordinate and thus only deviations of the pressure forces are calculated on the σ-co-ordinate. In this way, errors due to the co-ordinate transformation can be reduced.

The horizontal diffusion terms F_u, F_v and F_T in the majority of calculations are parametrized in terms of a biharmonic horizontal viscous term, although in the latter part of the paper the results from these calculations are compared with those using the Laplacian form. Details of the various frictional forms are well-known[18] and will be briefly discussed later in the paper.

We should point out that the use of a free surface model is not important in the problem considered in this paper and hence comparisons with the rigid lid model of CH93 are valid. This is because the barotropic forcing produced by changes in the free surface does not contribute to the generation of internal waves, which involve disturbances of the internal density surfaces. A time-splitting method is used to solve the model equations in order to reduce the computational time. Thus the velocity components u and v can be written as

$$u = \tilde{U} + u', \qquad v = \tilde{V} + v',$$

where $\tilde{U}$ and $\tilde{V}$ are the depth-mean velocities (external mode) and u' and v' are the depth-dependent velocities (internal mode). Since the external mode represents fast-moving gravity waves, a small time step is required for the time integration of the free surface wave which involves $\tilde{U}$ and $\tilde{V}$ in order to satisfy the CFL condition. The internal mode, however, represents slow-moving waves and hence much larger time steps can be used. To avoid errors in mass conservation due to the use of the time-splitting method, the sea surface elevation is recomputed before the internal mode equations are integrated by using the depth-mean velocity computed from the time mean of that determined with smaller time steps. The vertical velocity ω is therefore calculated from

$$\frac{\partial Hu'}{\partial x} + \frac{\partial Hv'}{\partial y} + \frac{\partial H\omega}{\partial\sigma} = 0. \tag{9}$$

A staggered Arakawa C finite difference grid is employed in the horizontal, with discretization in the vertical accomplished by a standard finite difference grid in σ-co-ordinates. The vertical diffusion terms, determined using a range of turbulence energy models, are computed by a fully implicit scheme. Details of the numerical method have been presented elsewhere[22–25] and will not be repeated here.

2.2. *Turbulence Kinetic Energy (TKE) models*

The vertical eddy viscosity and diffusivity in the model are calculated using a range of turbulence kinetic energy (TKE) models. In particular, we are interested in two types of TKE models: (i) a two-equation model which involves two prognostic equations for the turbulence energy and the length scale and (ii) a simpler and computationally less expensive one-equation model which involves one prognostic equation for the turbulence energy and a specified length scale. We are also interested in the contribution of each term in the equations to the turbulence energy budget. The major features of the models are outlined next.

2.2.1. Two-equation ($q^2 - q^2\imath$) TKE model. This model, which was developed by Mellor and Yamada[19,26] and used by, among others, Blumberg and Mellor[27] and recently by Oey and Chen[28] and Xing and Davies,[29] involves an equation for q^2, where $q^2 = 2E$, with E the turbulence kinetic energy (TKE). In σ-co-ordinates this takes the form

$$\begin{aligned}&\frac{\partial q^2 H}{\partial t} + \nabla \cdot (Hq^2\mathbf{V}) + \frac{\partial Hq^2\omega}{\partial \sigma}\\&\quad = 2\frac{K_{\mathrm{m}}}{H}\left[\left(\frac{\partial u}{\partial \sigma}\right)^2 + \left(\frac{\partial v}{\partial \sigma}\right)^2\right] + \frac{2gK_{\mathrm{h}}}{\rho_0}\frac{\partial \rho}{\partial \sigma} - \frac{2q^3H}{B_1\imath} + \frac{1}{H^2}\frac{\partial}{\partial \sigma}\left(S_q q\imath\frac{\partial q^2 H}{\partial \sigma}\right) + HF_q. \end{aligned} \tag{10}$$

The first term on the left is the time variation of turbulence energy, with the next two terms representing its advection. On the right the first term represents the vertical shear production of turbulence energy. The second term is the suppression of turbulence due to stratification and the third term determines the rate of loss of turbulence energy be dissipation processes. The vertical and the horizontal diffusion are represented by the last two terms in the equation. The various coefficients used in the equation are given later.

The equation for the length scale $\imath$ in σ-co-ordinates takes the form

$$\begin{aligned}&\frac{\partial q^2\imath H}{\partial t} + \nabla \cdot (Hq^2\imath\mathbf{V}) + \frac{\partial Hq^2\imath\omega}{\partial \sigma}\\&\quad = \frac{\imath E_1 K_{\mathrm{m}}}{H}\left[\left(\frac{\partial u}{\partial \sigma}\right)^2 + \left(\frac{\partial v}{\partial \sigma}\right)^2\right] + \frac{\imath E_1 g K_{\mathrm{h}}}{\rho_0}\frac{\partial \rho}{\partial \sigma} - \frac{q^3}{B_1}WH + \frac{1}{H}\frac{\partial}{\partial \sigma}\left(S_q q\imath\frac{\partial q^2\imath}{\partial \sigma}\right) + HF_\imath, \end{aligned} \tag{11}$$

with W a wall proximity function defined by

$$W = 1 + E_2\left(\frac{1}{\kappa L}\right)^2, \tag{12}$$

where L is given by

$$L^{-1} = (\zeta - z)^{-1} + (H + z)^{-1} \tag{13}$$

and $\kappa = 0{\cdot}4$ is the Von Karman constant.

The vertical eddy viscosity and eddy diffusivity are computed from

$$K_{\mathrm{m}} = \imath q S_{\mathrm{M}}, \qquad K_{\mathrm{h}} = \imath q S_{\mathrm{H}}, \tag{14}$$

with S_M and S_H the stability functions given by Galperin *et al.*[30] as

$$S_{\mathrm{H}} = \frac{A_2(1 - 6A_1/B_1)}{1 - 3A_2(B_2 + 6A_1)G_{\mathrm{H}}}, \tag{15}$$

$$S_{\mathrm{M}} = \frac{A_1\{1 - 3C_1 - 6A_1/B_1 - 3A_2G_{\mathrm{H}}[(B_2 - 3A_2)(1 - 6A_1/B_1) - 3C_1(B_2 + 6A_1)]\}}{[1 - 3A_1G_{\mathrm{H}}(6A_1 + B_2)](1 - 9A_1A_2G_{\mathrm{H}})}, \tag{16}$$

where $G_{\mathrm{H}} = -\ell^2N^2/q^2$ is the buoyancy flux, with N the buoyancy frequency. The coefficients used in equations (10)–(16) are given by $A_1 = 0{\cdot}92, A_2 = 0{\cdot}74, B_2 = 10{\cdot}1, C_1 = 0{\cdot}08, S_q = 0{\cdot}2, B_1 = 16{\cdot}6$ and $E_1 = 1{\cdot}33$. Following Galperin *et al.*[31] a limiting condition is applied to the length scale of the form

$$\ell \leqslant k_1 q/N, \tag{17}$$

where k_1 is a constant determined in terms of laboratory and observational data.

The above turbulence closure model is often called the Mellor–Yamada level 2·5 model and is widely used in the modelling of geophysical flow.[19,26] The empirical constants have mainly been determined from laboratory observations and appear to be valid across a range of situations, including ocean circulation models[27] and numerical weather prediction models.[32,33] The importance of limiting the mixing length using (17) and its influence upon the solutions are discussed in References 31 and 34.

2.2.2. One-equation TKE model. This turbulence energy closure model is similar to the two-equation model in concept but different in detail. It involves one prognostic equation for the TKE, denoted E, and an algebraic form for the length scale ℓ.[20] The TKE equation in σ-co-ordinates takes the form

$$\begin{aligned}\frac{\partial HE}{\partial t} &+ \nabla \cdot (HE\mathbf{V}) + \frac{\partial HE\omega}{\partial \sigma}\\ &= \frac{K_{\mathrm{m}}}{H}\left[\left(\frac{\partial u}{\partial \sigma}\right)^2 + \left(\frac{\partial v}{\partial \sigma}\right)^2\right] + \frac{g}{\rho_0}K_{\mathrm{h}}\frac{\partial \rho}{\partial \sigma} - \varepsilon H + \frac{\beta_0}{H^2}\frac{\partial}{\partial \sigma}\left(K_{\mathrm{h}}\frac{\partial HE}{\partial \sigma}\right) + HF_e,\end{aligned} \tag{18}$$

where β_0 is a specified constant. The turbulence dissipation ε and the vertical eddy viscosity or diffusivity (taken to be equal) are calculated from

$$\varepsilon = C_1E^{3/2}/\ell, \qquad K_{\mathrm{m}} = C_0E^{1/2}, \tag{19}$$

where $C_0 = C^{1/4}, C_1 = C_0^3$ and $C = 0{\cdot}06$.

In this one-equation model the length scale can be determined in a number of different ways. One simple formulation is a trigonometric type of length scale, namely a parabola of the form

$$\ell = \frac{1}{1/\ell_1 + 1/\ell_2}, \qquad \ell_1 = \kappa(\sigma H + z_0)\exp(\beta_1\sigma), \qquad \ell_2 = \kappa(H - \sigma H + z_{\mathrm{s}}), \tag{20}$$

where $\kappa = 0{\cdot}4$ is the Von Karman constant, β_1 is an empirical coefficient, z_0 is the bed roughness length and z_{s} is a surface roughness length which controls the value of ℓ at the sea surface.

The above formulation of the TKE closure scheme including the length scale has been used in a number of shallow water simulations.[23–25] In the application in this paper, however, the length scale can be unreasonably large in the deep water environment. Therefore a limiting condition similar to (17) is applied to the length scale (20).

2.2.3. Eddy viscosity related to the Richardson number. In addition to the TKE models described above, a simple Richardson-number-dependent eddy viscosity and eddy diffusivity are also used, since this simple model is popular in oceanography. Following Munk and Anderson,[21] the eddy viscosity and eddy diffusivity take the form

$$K_{\mathrm{m}} = A_{\mathrm{r1}}\psi_1 + B_{\mathrm{r1}}, \tag{21}$$

$$K_{\mathrm{h}} = A_{\mathrm{r2}}\psi_2 + B_{\mathrm{r2}}, \tag{22}$$

where ψ_1 and ψ_2 are the Richardson-number-dependent stability functions given by

$$\psi_1 = (1 + 10Ri)^{-1/2}, \tag{23}$$

$$\psi_2 = (1 + 3{\cdot}3Ri)^{-3/2}. \tag{24}$$

Here $A_{\mathrm{r1}}, B_{\mathrm{r1}}, A_{\mathrm{r2}}$ and B_{r2} are constants and Ri is the Richardson number defined by

$$Ri = -\frac{(gH/\rho_0)(\partial\rho/\partial\sigma)}{(\partial u/\partial\sigma)^2 + (\partial v/\partial\sigma)^2}. \tag{25}$$

2.3. *Formulation of the horizontal diffusion*

Two types of horizontal diffusion are considered here, i.e. the Laplacian form and the biharmonic form, both of which are computed on σ-surfaces. The Laplacian form is given (using F_u for illustrative purposes, with F_v and F_T formulated in an identical way) by

$$F_u = A_{\mathrm{M}}\nabla^2 u = A_{\mathrm{M}}\left(\frac{\partial^2 u}{\partial x^2} + \frac{\partial^2 u}{\partial y^2}\right). \tag{26}$$

For the biharmonic form we have

$$F_u = -B_{\mathrm{M}}\nabla^4 u = -B_{\mathrm{M}}\left(\frac{\partial^4 u}{\partial x^4} + 2\frac{\partial^4 u}{\partial x^2 \partial y^2} + \frac{\partial^4 u}{\partial y^4}\right). \tag{27}$$

Here A_{M} and B_{M} are the coefficients for momentum diffusion. The coefficients for heat and turbulence energy diffusion (A_{H} and B_{H}) are set equal to that for momentum. Previous work[18] shows that the use of a biharmonic formulation of diffusion enables the computational noise to be controlled without imposing unrealistically high damping on the larger features of the flow. We shall show the influences of the different diffusion formulations on internal lee waves later in the paper.

2.4. *Boundary conditions*

At the sea surface there is no applied wind stress or heat flux, so the boundary condition for velocity and temperature at the sea surface takes the form

$$\frac{\partial u}{\partial\sigma} = \frac{\partial v}{\partial\sigma} = \frac{\partial T}{\partial\sigma} = 0. \tag{28}$$

For the TKE models the sea surface boundary condition states that there is no turbulence flux through the sea surface and takes the form

$$\frac{\partial E}{\partial\sigma} = 0. \tag{29a}$$

For the two-equation model the length scale at the sea surface is given by

$$lq^2 = z_s q^2, \tag{29b}$$

where z_s is the sea surface roughness length.

At the sea bed we use a linear bottom friction condition which takes the form

$$\frac{K_m}{H}\frac{\partial u}{\partial \sigma} = C_d u, \qquad \frac{K_m}{H}\frac{\partial v}{\partial \sigma} = C_d v, \tag{30a}$$

with C_d the coefficient of the bottom friction. For the temperature equation there is no flux through the sea bed, so

$$\frac{\partial T}{\partial \sigma} = 0. \tag{30b}$$

For the TKE model we use a boundary condition including the balance of the turbulence production, dissipation and diffusion given by Xing and Davies,[29] namely

$$\frac{\partial E}{\partial \sigma} = \frac{C_0 C_1 E^2 H}{\beta_0 K_m^2} - \frac{u_*^4 \Delta_\sigma H}{\beta_0 K_m^2}. \tag{31}$$

Here Δ_σ is the lowest model level height and u_* is the friction velocity. A bottom boundary condition for q^2 is formed in a similar way, with the length scale specified as the bottom roughness length at the sea bed.

2.5. Set-up of the numerical experiments

The model domain is identical with that used by CH93, namely a straight channel with inflow at its south end and outflow at the north and with solid side walls at the west and east. Along the side wall boundaries the component of flow normal to the wall and the heat flux are taken as zero. At the open boundaries we must ensure that the imposed inflow and any disturbances generated in the model domain pass through the boundaries (in particular the downstream boundary) without serious reflection. This is achieved by applying an Orlanski radiation boundary condition for the temperature, with enhanced horizontal diffusion near the boundary zone. A simple radiation boundary condition is used for the barotropic flow (sea surface elevation). The numerical results show that with these open boundary conditions the influence of the boundary on the internal area is negligible. The location of the seamount was identical with that used by CH93 and its form is described later.

The initial objective of the calculations was to ensure that the finite difference model developed here was as accurate as the spectral model of CH93 and then to take advantage of the fact that with the finite difference approach we can examine the enhancement of the turbulence mixing downstream of the seamount due to the generation of internal lee waves. The magnitude of the various terms in the turbulence energy equations will also be examined in order to understand the mechanisms producing the enhanced levels of turbulence. In addition, comparisons will be made with the simpler models to see whether the main physical processes can be reproduced by these computationally less expensive models. Finally, the near-bottom processes, which are of importance to sediment transport and biological processes, will also be discussed.

In most of the numerical experiments presented in this paper, the bottom topography is an isolated bell-shaped circular seamount, so the water depth $h(x, y)$ takes the form

$$h(x, y) = H_0 - h_0\left[1 + \left(\frac{r}{a}\right)^2\right]^{-3/2}, \tag{32}$$

where $r^2 = (x - x_0)^2 + (y - y_0)^2$, a is the horizontal scale of the seamount, h_0 is the maximum seamount height centred at (x_0, y_0) and H_0 is the water depth over the flat bottom. This profile has been widely used in the study of the atmospheric flow over mountains, since it is convenient for a linear analytic solution because of the simple form of the Fourier transformation.[8]

A Gaussian-shaped seamount has been used in the oceanographic literature.[15,36] A comparison will be made in this paper with different seamount profiles in order to examine their influence on internal waves and associated turbulence, namely a bell-shaped seamount, a Gaussian-shaped seamount and a cosine-squared form of seamount. The Gaussian-shaped seamount takes the form

$$h(x, y) = H_0 - h_0 e^{-r^2/a^2} \tag{33}$$

and the cosine-squared seamount has the form

$$h(x, y) = H_0 - h_0 \left\{ \frac{1}{2} \left[1 + \cos\left(\frac{r\pi}{2a}\right) \right] \right\}^2, \qquad r \leqslant 2a. \tag{34}$$

The three different seamount profiles are shown in Figure 1. It can be seen that the cosine-squared seamount (as defined by (34)) has the steepest slope near the bottom. The bell-shaped seamount has the gentlest slope near the bottom. As we shall see in the next section, this has a significant effect on the flow and turbulence mixing near the bottom of the seamount.

The numerical calculations were carried out using a horizontal grid of 76 × 98 points with a finite difference grid of 5 km in both the x- and the y-direction. There are 25 irregular vertical σ-levels with a relatively higher resolution near the bottom. Each calculation begins from rest. A spatially uniform inflow U_i both in the horizontal and vertical is imposed at the southern open boundary and held fixed. After about 10 days integration the interior flow reaches the steady state. The time step is 400 s for the internal mode and 10 s for the external mode.

In addition to the form of the seamount, four non-dimensional numbers determine the steady state flow, namely the Froude number $F = U_i/NH_0$, with U_i the specified input current, the Burger number $S = NH_0/fa$, the fractional seamount height $\delta = h_0/H_0$ and the aspect ratio $\Delta = H_0/a$. The Froude number defined here can be explained as the ratio of the imposed background velocity to the phase speed of the lowest-mode internal wave. The Burger number is a measure of the strength of the stratification. A detailed study of the influence of Froude number upon internal lee wave generation over a Gaussian seamount can be found in CH93 and has been used to check the model developed here and the accuracy of the open boundary outflow condition. In order to determine the accuracy of the model and the boundary conditions, an initial series of calculations was performed without

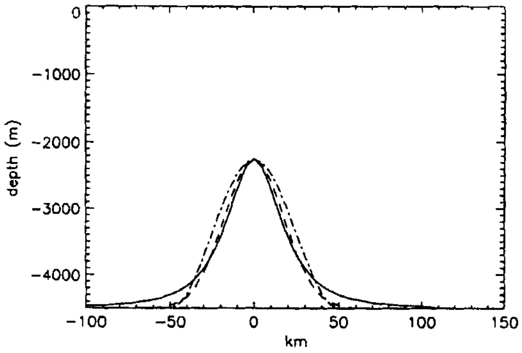

Figure 1. Three different seamount profiles used in experiments: full line, bell-shaped; broken line, Gaussian-shaped; chain line, cosine-squared. In this figure the fractional seamount height $\delta = h_0/H_0$ is 0·5

vertical diffusion and bottom friction and with only minimum horizontal friction (in order to obtain a stable solution), namely the parameter settings used in CH93. Despite the differences in model formulation, i.e. the finite difference approach in the vertical with a free surface used here and the spectral model used in CH93, the results were indistinguishable from those of CH93 and hence will not be reported here. Having satisfied the primary aim of the numerical calculations, namely to check that the model was sufficiently accurate to reproduce the features of CH93, we will be concerned in the rest of the paper with addressing problems that could not be considered in CH93, namely examining the mixing produced by the internal lee waves and the effects of seamount topography upon the mixing. In subsequent calculations we will fix N, H_0, a, f and U_i at $N = 5{\cdot}556 \times 10^{-4}\ \mathrm{s}^{-1}, H_0 = 4500\ \mathrm{m}, a = 25 \times 10^3\ \mathrm{m}, f = 10^{-4}\ \mathrm{s}^{-1}$ and $U_i = 0{\cdot}5\ \mathrm{m\ s}^{-1}$. Thus the aspect ratio and Burger number are fixed at $\Delta = 0{\cdot}18$ and $S = 1$ respectively, representing a thin ocean and a dynamically strong stratification. With $U_i = 0{\cdot}5\ \mathrm{m\ s}^{-1}$ the Froude number is equal to 0·2. Three different maximum seamount heights h_0 are used in our experiments, representing small ($\delta = 0{\cdot}3$), medium ($\delta = 0{\cdot}5$) and large ($\delta = 0{\cdot}75$) amplitudes of seamount. Therefore the Froude numbers F' based on the maximum seamount height ($F' = U_i/Nh_0$) are 0·67, 0·4 and 0·27 respectively. This seamount-height-based Froude number is a measure of the non-linearity of the flow over the seamount.

3. INTERNAL LEE WAVES AND WAVE-ENHANCED TURBULENCE MIXING OVER AN ISOLATED SEAMOUNT

3.1. *Linear theory*

Before we discuss the results of the numerical experiment, it is helpful to review some simple linear theory on internal lee waves over a seamount. Following CH93, in a simple linear two-dimensional (x–z) system, assuming constant uniform inflow velocity U_i and buoyancy frequency N and spatically varying velocity u of the form

$$u = \tilde{u}_h(x)\cos(n\pi z/H_0), \tag{35}$$

where n is the vertical mode number and $\tilde{u}_h(x)$ is the horizontal variation in u, the governing equation takes the form (dropping the subscript 'h' for convenience)

$$\frac{B_M U_i}{(NH_0)^2}\frac{\partial^5 \tilde{u}}{\partial x^5} + \left(F^2 - \frac{1}{(n\pi)^2}\right)\frac{\partial^2 \tilde{u}}{\partial x^2} + \frac{f^2}{(NH_0)^2}\tilde{u} = 0, \tag{36}$$

where B_M is the coefficient of biharmonic diffusion and F is the Froude number. Assuming $\tilde{u} \sim \exp(-\lambda x)$, the solution for λ can be obtained by solving a fifth-order polynomial equation of the form

$$\frac{B_M U_i}{(NH_0)^2}\lambda^5 - \left(F^2 - \frac{1}{(n\pi)^2}\right)\lambda^2 - \frac{f^2}{(NH_0)^2} = 0. \tag{37}$$

For an inviscid flow ($B_M = 0$) we have the dispersion relation

$$k^2 = \frac{(f/NH_0)^2}{F^2 - 1/(n\pi)^2}, \tag{38}$$

where k is the wave number (imaginary part of λ). For an internal lee wave to exist, λ must be real and this requires the flow to be supercritical for mode n, i.e.

$$F > \frac{1}{n\pi} \quad (= F_c). \tag{39}$$

For a mode 1 wave $F_c \approx 0{\cdot}32$ and for a mode 2 wave $F_c \approx 0{\cdot}16$. Based on these values, in our case we expect that internal lee waves cannot be generated, since the Froude number computed with $U_i = 0{\cdot}5$ m s^{-1} has a value of 0·2, which is below the critical Froude number $F_c(0{\cdot}32)$. However, CH93 have shown some examples in which mode 1 internal lee waves could be generated near the seamount in the case of $F = 0{\cdot}3$, which is smaller than F_c owing to the local acceleration of the flow over the seamount. Consequently, as we will show, internal lee waves are also generated in our calculation owing to the non-linear local acceleration. In subsequent calculations we will determine the wavelengths of the lee waves in the numerical simulations and compare them with the wavelengths computed from linear theory. For the parameters used here, the wavelength for mode 2 is about 20 km and for mode 3 about 27 km.

From the solution of (37), CH93 demonstrated that the wavelength (imaginary part of λ) an decay distance (real part of λ) decreased as the Froude number decreased (Figure 14 of CH93). For small F the decay distance decreases more rapidly than the wavelength, which indicates that the internal lee waves are rapidly dissipated by subgrid-scale horizontal mixing. Consequently, as we will show, the parametrization of the horizontal mixing term has a significant influence upon the horizontal variation in the internal lee waves.

3.2. *Results from the two-equation turbulence model*

Initially a number of numerical experiments were performed with the two-equation turbulence model for the vertical eddy viscosity and diffusivity. For the horizontal diffusion we use the biharmonic formulation with the same value of the diffusion coefficients for momentum and temperature. From the numerical calculations the high seamount requires a larger value of minimum horizontal diffusion to obtain a numerically stable solution. We use $B_M = B_H = 3{\cdot}2 \times 10^9$ m^4 s^{-1}. Reducing B_M and B_H to $1{\cdot}6 \times 10^9$ m^4 s^{-1}, the model becomes unstable for the case of $\delta = 0{\cdot}75$, although it is stable for the cases of $\delta = 0{\cdot}3$ and 0·5.

Figure 2 shows the contours of density (here denoted by σ_t, where $\sigma_t = \rho - \rho_0$), vertical velocity w (see figure caption for details of contour interval) and velocity v (which we will term the streamwise velocity since it is in the direction of the imposed flow U_i) taken along the channel from south (left side, where the model is forced with the input velocity U_i) to north through the centre of the seamount after the model has reached a steady state. The spin up to the steady state is achieved by starting the model with a horizontal uniform density field with a vertical variation determined by N and a zero flow field. Motion in the system is then induced by specifying a uniform inflow velocity U_i at the southern end of the channel (the left-hand side of the cross-sections shown in the figure) and integrating forwards in time until a new steady state is obtained (approximately 10 days). For the calculation shown in Figure 2 the seamount height is $\delta = 0{\cdot}3$, which represents a small amplitude of seamount. From the vertical velocity plot there is no clear evidence of mode 1 internal lee waves over the seamount because of the small Froude number. It seems that both mode 2 and mode 3 internal waves exist and the wavelength of the waves is of the order of 25 km, which compared well with the linear theory results of about 20 km for mode 2 waves and 27 km for mode 3 waves. It is interesting to point out that, owing to the relatively large background current velocity and the small amplitude of the seamount, the water flows over the seamount rather than forming a Taylor cap.[36] The cold higher-density water on the upstream side of the seamount is advected to the crest of the seamount by the

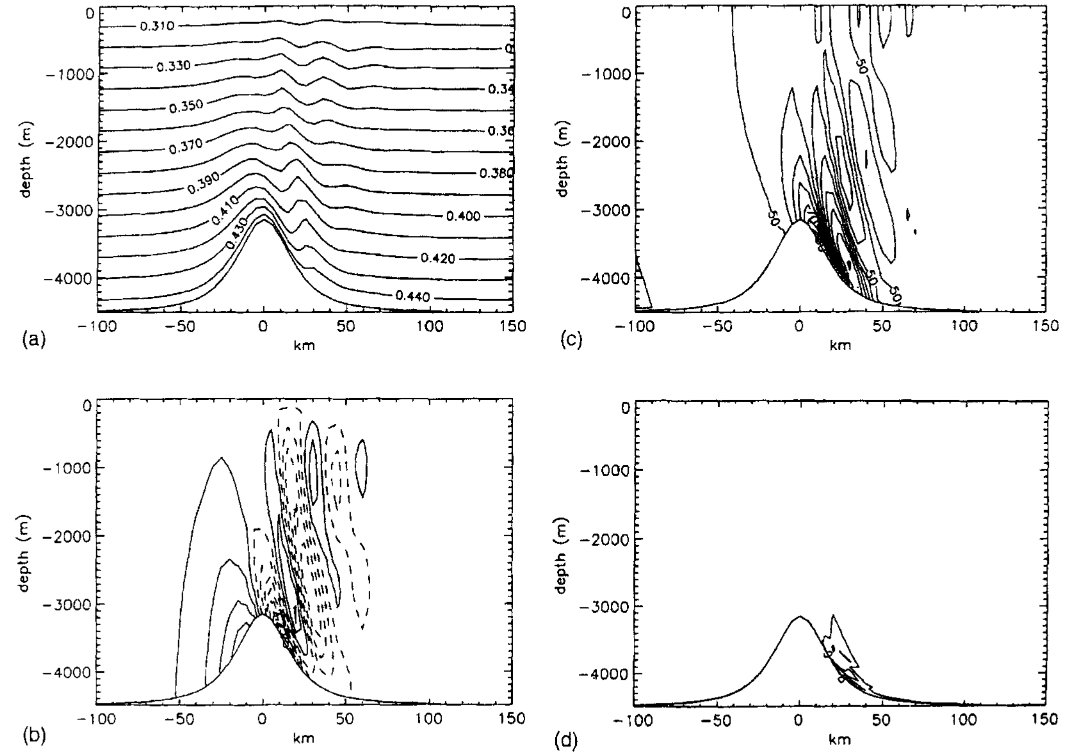

Figure 2. Vertical sections of (a) density anomaly denoted by $\sigma_t = \rho - \rho_0$ (kg m^{-3}), (b) vertical velocity w, (c) velocity v (termed streamwise velocity) and (d) TKE taken through centre of seamount in direction of external flow. The density contour interval is 0·01 kg m^{-3}. The vertical velocity contours begin with ±0·25 cm s^{-1} with an interval of 0·5 cm s^{-1} (broken lines are downwelling and full lines are upwelling). The streamwise velocity v is in cm s^{-1} with an interval of 5 cm s^{-1}. The TKE contours are in $\log_{10}$(m^2 s^{-2}). A bell-shaped seamount with $\delta = 0{\cdot}3$ was used in the calculation

upwelling and then to the lee side of the seamount by the downwelling. This results in a stronger vertical density gradient near the bottom over the lee side of the seamount. The turbulence kinetic energy (TKE) is very small in this case and the maximum TKE is of the order of 10^{-8} m^2 s^{-2}. The computed vertical eddy viscosity and eddy diffusivity (not shown here) are smaller than the molecular viscosity ($1{\cdot}4 \times 10^{-6}$ m^2 s^{-1}).

As the seamount height increases, we expect that the amplitude of the internal lee waves will increase. In Figure 3 we show the internal lee waves over a seamount with $\delta = 0{\cdot}5$. Figure 3(a) shows the vertical section of density through the centre of the seamount. The internal displacement of the density is much larger in this case than in the case of $\delta = 0{\cdot}3$. Figures 3(b)–(e) show the vertical sections of vertical velocity, streamwise velocity, TKE and eddy viscosity respectively taken along the channel through the centre of the seamount in the direction of the imposed external flow from south (left of figure) to north. Compared with the case of $\delta = 0{\cdot}3$ (Figure 2), the structure of the internal lee waves is similar. The wave amplitude, however, is much larger, as shown in the vertical velocity plot. The maximum upwelling velocity is about 2·5 cm s^{-1} in this case, which is two times larger than that in the case of $\delta = 0{\cdot}3$. Figure 3(d) shows strong TKE over the lee side of the seamount. The maximum TKE, occurring near the upwelling centre, is over 10^{-2} m^2 s^{-2}. The computed vertical eddy viscosity can be very large in this region, as shown in Figure 3(e), with a maximum vertical eddy viscosity of over 1 m^2 s^{-1}. The vertical eddy diffusivity (not shown here) has a similar value.

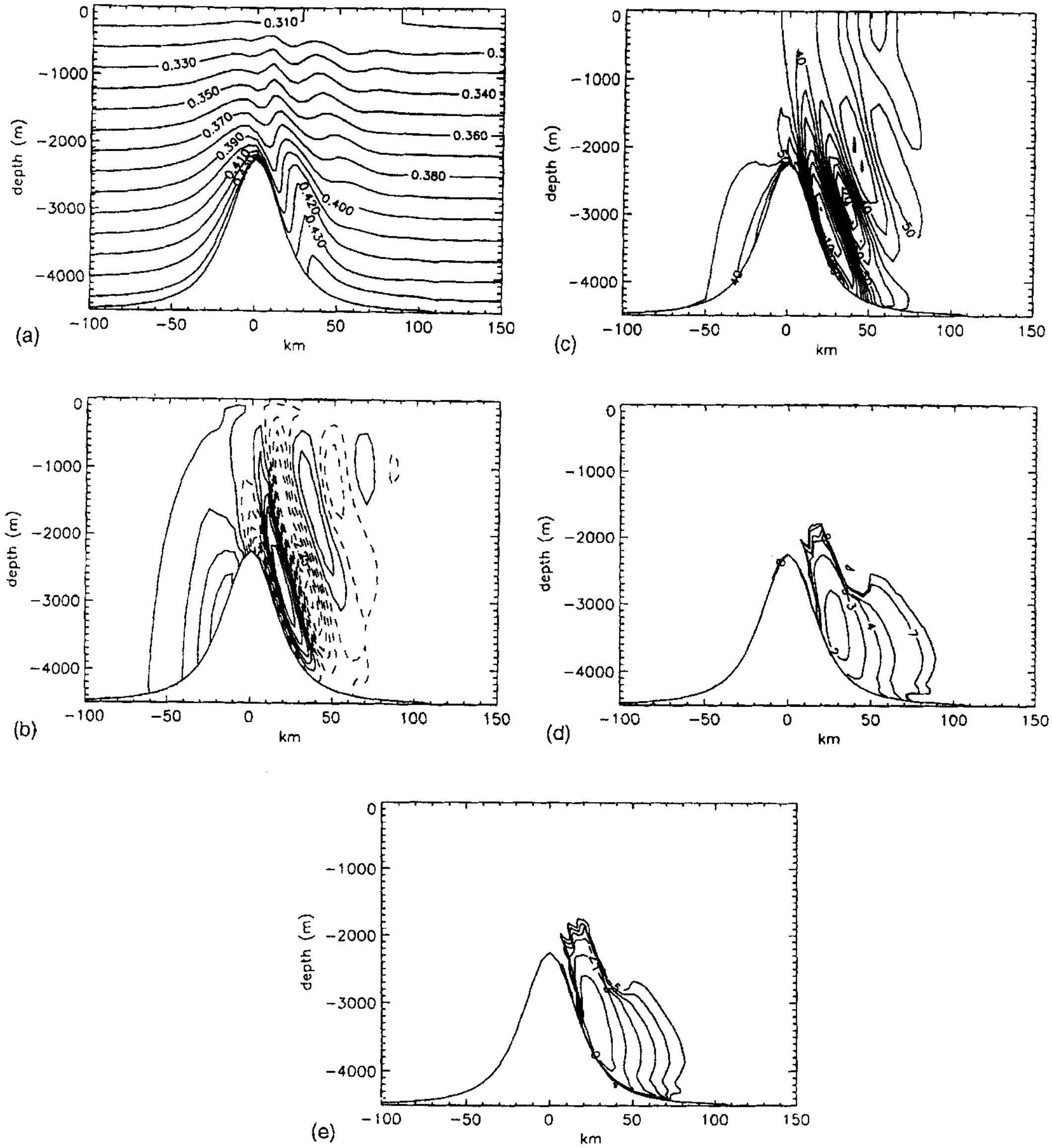

Figure 3. As in Figure 2, but for $\delta = 0{\cdot}5$. Figure 3(e) shows the vertical eddy viscosity (contours in $\log_{10}(\mathrm{m}^2\ \mathrm{s}^{-1})$)

In Figure 4 we show the contours of horizontal distributions of vertical velocity, TKE and vertical eddy viscosity at a depth of 2500 m. The peak upwelling velocity decays from about 2·5 cm s^{-1} on the lee side of the seamount to about 1·25 cm s^{-1} at a position 40 km downstream from the seamount centre and further downstream to about 0·25 cm s^{-1}. CH93 suggested that this downstream decay of internal lee waves is due to two factors—slowing of the ambient current and subgrid-scale mixing—both of which contribute here. From Figure 4 we note that both the TKE and the eddy viscosity have similar distributions to the vertical velocity. The maximum TKE on the lee side is of the order of 10^{-3} m^2 s^{-2} and decays to 10^{-6} m^2 s^{-2} at 40 km downstream of the seamount centre. Similarly, the maximum eddy viscosity is of the order of 10^{-1} m^2 s^{-1} on the lee side of the seamount and decreases to 10^{-4} m^2 s^{-1} at 40 km downstream from the centre of the seamount.

The TKE balance analysis gives us further insight into the processes producing the internal-lee-wave-induced turbulence mixing. In the steady state the turbulence energy equation reduces to

$$2\frac{K_m}{H}\left[\left(\frac{\partial u}{\partial \sigma}\right)^2+\left(\frac{\partial v}{\partial \sigma}\right)^2\right]+\frac{2gK_h}{\rho_0}\frac{\partial \rho}{\partial \sigma}-\frac{2q^3H}{B_1 l}-\left(\nabla\cdot(Hq^2\mathbf{V})+\frac{\partial Hq^2\omega}{\partial \sigma}\right)$$
$$+\frac{1}{H^2}\frac{\partial}{\partial \sigma}\left(S_q q l\frac{\partial q^2 H}{\partial \sigma}\right)+HF_q=0. \tag{40}$$

A turbulence model using the balance of the first three terms on the left of the above equation (i.e. shear production, buoyancy suppression and viscous dissipation) is often called the Mellor–Yamada level 2 closure scheme.[19] This form of turbulence energy model is widely used in the literature because of the reduced computational overhead[37] compared with the full turbulence energy model. Here we have used a full prognostic turbulence energy equation since we anticipate the complexity of the flow in some of the applications of the model, e.g. steep bottom topography, and also because we wish to examine the relative importance of all the terms and compare results with simpler models.

In Figure 5 we show the vertical sections of various terms in the TKE balance equation (40) taken along the channel through the centre of the seamount. On the lee slope of the seamount the main balance of the TKE is the vertical shear production (Figure 5(a)) and the viscous dissipation (Figure 5(c)), both of which have maxima of the order of 10^{-2} m^3 s^{-3}. The stable stratification always acts as a buoyancy suppression term in the TKE balance and has a maximum value of the order of 10^{-3} m^3 s^{-3} (Figure 5(b)). It is interesting to note that the maximum of the suppression due to density is on the lee slope where the maximum TKE occurs. In fact, strong vertical mixing and upwelling motion reduces the stratification, which should reduce the suppression of turbulence by

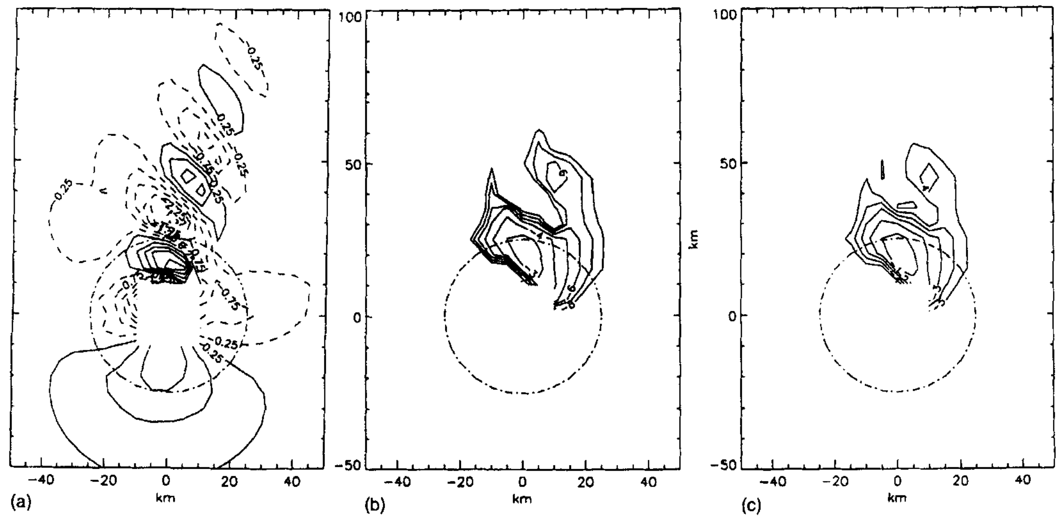

Figure 4. Contours of (a) vertical velocity, (b) TKE and (c) vertical eddy viscosity at a depth of 2500 m. The chain circle represents a seamount with $r = a$. The vertical velocity contours begin with ±0·25 cm s^{-1} with an interval of 0·5 cm s^{-1} (broken lines are downwelling and full lines are upwelling). The interval of TKE and eddy viscosity contours is $\log_{10}$(m^2 s^{-1}). A bell-shaped seamount with $\delta = 0{\cdot}5$ was used in the calculation

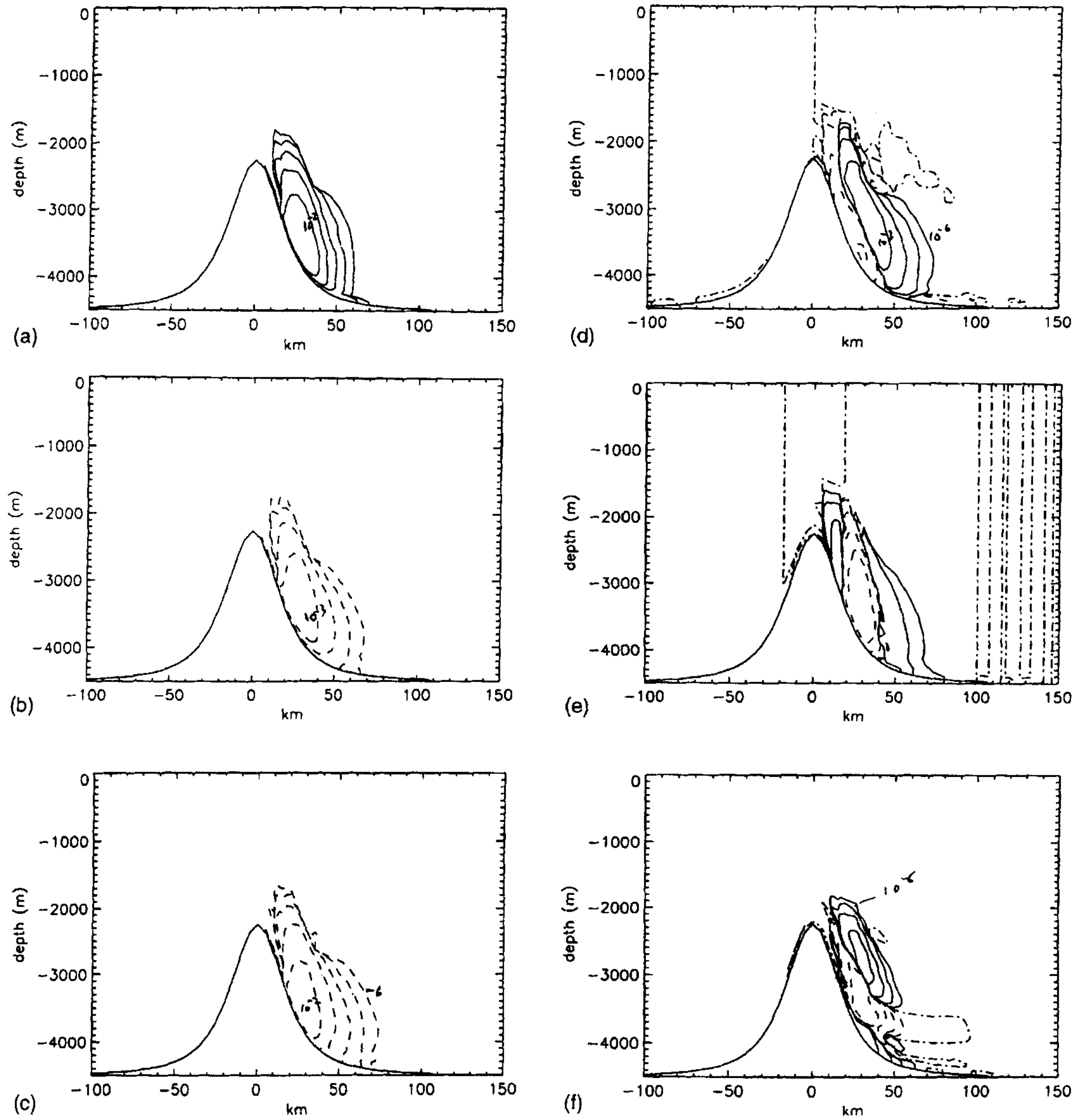

Figure 5. Vertical sections of various terms in turbulence energy balance equation (40) taken through centre of seamount (all in $\log_{10}(\mathrm{m}^3\ \mathrm{s}^{-3})$): (a) turbulence shear production; (b) density (buoyancy) suppression; (c) viscous dissipation; (d) advection of TKE; (e) vertical diffusion; (f) horizontal diffusion. A bell-shaped seamount with $\delta = 0{\cdot}5$ was used in the calculation

density. The effect due to the increase in the eddy diffusivity, however, is greater than that due to the density change. It is also interesting to note that the advection of the TKE has a significant effect on the TKE balance, since it is of at least the same order as the density (buoyancy) term. The vertical diffusion (Figure 5(e)) of the TKE also has an order of $10^{-3}\ \mathrm{m}^3\ \mathrm{s}^{-3}$ in the region of strong internal lee waves and hence cannot be neglected. However, the horizontal diffusion (Figure 5(f)) of the TKE is much smaller and not particularly important and could be neglected.

As the seamount height increases further to $\delta = 0{\cdot}75$, there are significant changes in the flow and internal lee wave patterns. Figure 6 shows the vertical sections of density, vertical velocity, streamwise velocity, TKE and viscosity taken along the channel through the centre of the seamount. In this case the flow is more effectively blocked by the seamount compared with the previous cases. On the upstream slope the maximum upwelling velocity is about 1·25 cm s^{-1}, compared with the maximum upwelling of 1·75 cm s^{-1} in the previous cases. More importantly, the downwelling on the lee slope is very small and limited to the upper 300 m of the seamount, with strong upwelling of maximum velocity about 3·5 cm s^{-1} occurring on the lee side below 3000 m. The important feature of this case is that flow separation occurs on the lee side of the seamount (see Figure 6(c)). The

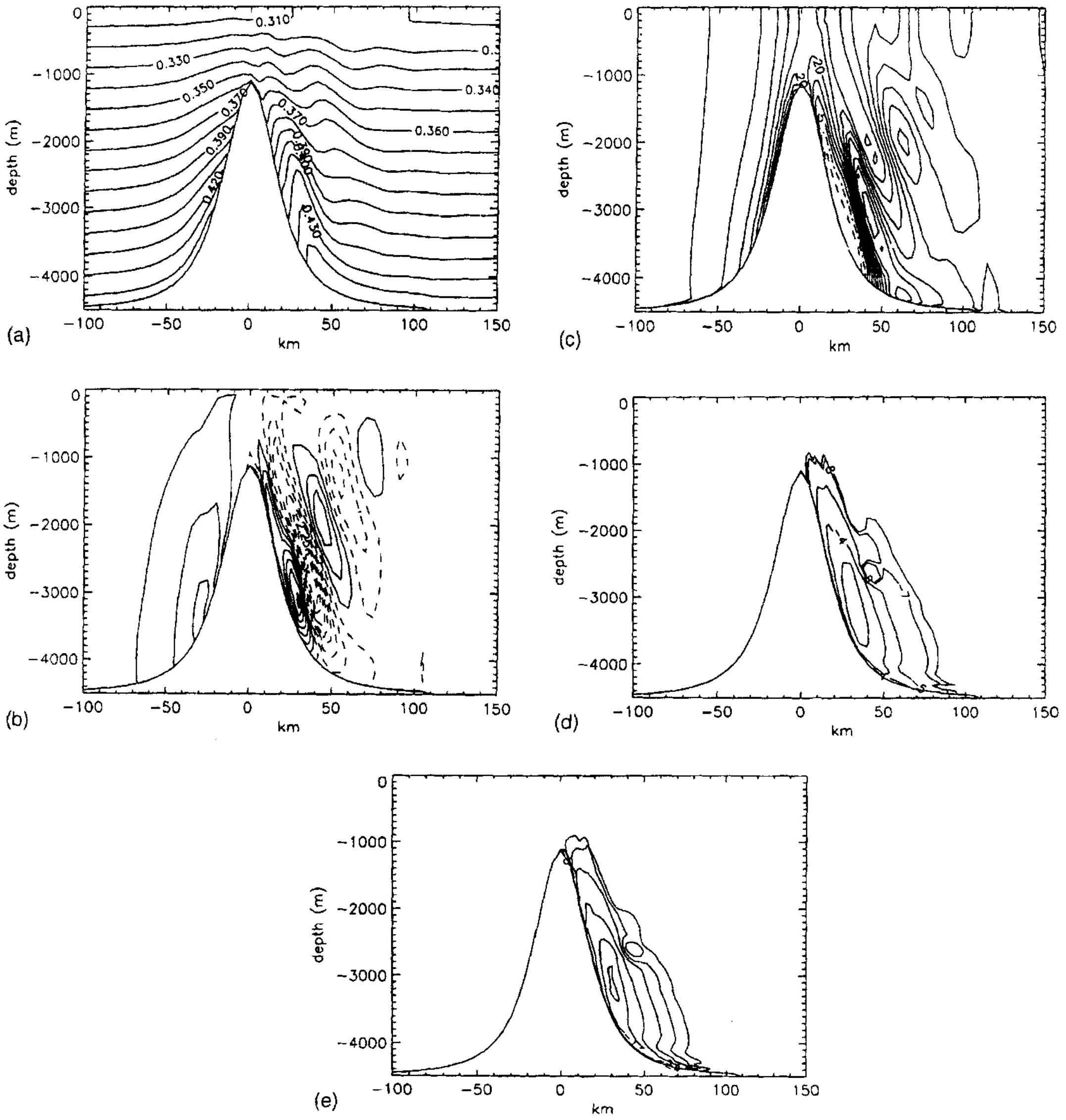

Figure 6. As in Figure 3, but for $\delta = 0{\cdot}75$

maximum reverse flow velocity is more than 10 cm s^{-1} (in the case of $\delta = 0{\cdot}5$, flow separation also occurs, although we cannot see it in the vertical section along the channel through the centre of the seamount owing to the asymmetric nature of the flow over the seamount). This flow separation is not boundary layer separation, since, when we repeat the case using a free slip condition between the water and the bottom surface, the flow separation over the lee slope of the seamount still exists. We suggest that the water behaves here very much like the atmospheric flow over an obstacle discussed by Smolarkiewicz and Rotunno,[38] although in our case rotation plays an important role. We shall return to this point later in this section.

The internal lee wave amplitude measured by the vertical velocity is larger in the case of $\delta = 0{\cdot}75$ than in the case of $\delta = 0{\cdot}5$. This differs from the results of CH93, who show that the maximum amplitude occurs at $\delta = 0{\cdot}5$. The reason for this is that we use the same value for the horizontal diffusions for different seamount heights. One interesting thing is that the computed TKE and eddy viscosity in the case shown in Figures 6(d) and 6(e) are not as large as those in the case of $\delta = 0{\cdot}5$. For example, the maximum TKE is of the order of 10^{-3} m^2 s^{-2}, compared with a maximum TKE of 10^{-2} m^2 s^{-2} in the case of $\delta = 0{\cdot}5$. The vertical eddy viscosity is in general smaller than that with $\delta = 0{\cdot}5$, although both have a similar value of the maximum (1 m^2 s^{-1}).

In Figure 7 we show plan views of the contours of vertical velocity, TKE and eddy viscosity at a depth of 2500 m. From a comparison of Figure 7(a) with Figure 4(a) it is evident that over the lee slope the vertical velocity for the case of $\delta = 0{\cdot}75$ is larger than for the case of $\delta = 0{\cdot}5$ and there is a phase difference between the two cases. The maximum upwelling for this case is at about 25 km downstream of the seamount centre, whereas in the case of $\delta = 0{\cdot}5$ the vertical velocity is much smaller. Further downstream the two cases have similar wave patterns. The TKE and eddy viscosity plots show that the maxima (of the order of 10^{-3} m^2 s^{-3} for TKE and 10^{-1} m^2 s^{-1} for eddy viscosity) are located further downstream compared with the case of $\delta = 0{\cdot}5$. The second maximum centre for TKE and eddy viscosity does not appear in this case, although it can be clearly seen in the case of $\delta = 0{\cdot}5$.

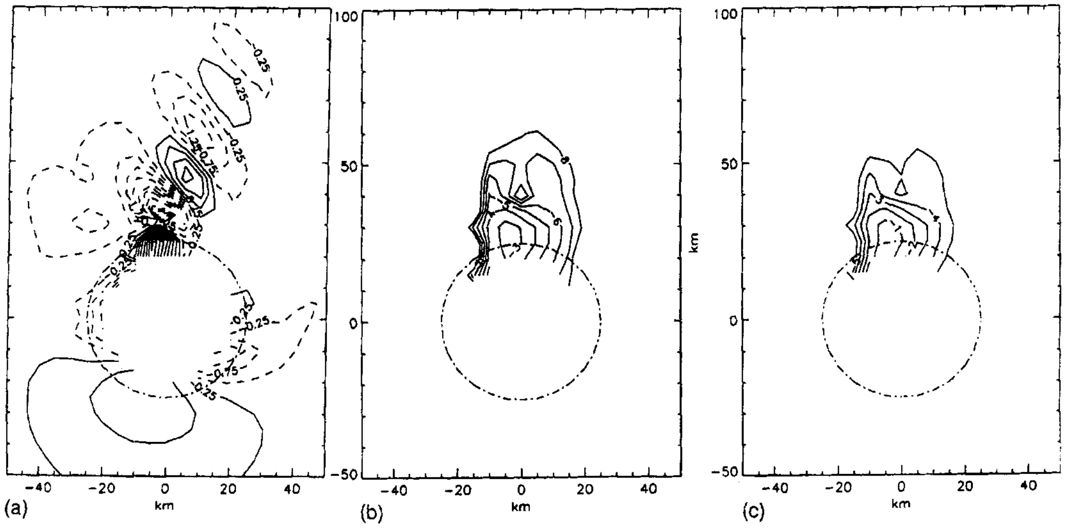

Figure 7. As in Figure 4, but for $\delta = 0{\cdot}75$

The turbulence energy balance for the case of $\delta = 0{\cdot}75$ is shown in Figure 8, which indicates that the main TKE balance terms are the shear production of TKE and the viscous dissipation. However, compared with the case of $\delta = 0{\cdot}5$, these two terms are much smaller, with a maximum of 10^{-3} m^3 s^{-3}. The maximum density suppression term is of the order of 10^{-4} m^3 s^{-3} as expected. One important feature in this case, however, is the strong turbulence energy advection over the lee slope, having a maximum of the order of 10^{-3} m^3 s^{-3}, which is the same order as the shear production of TKE.

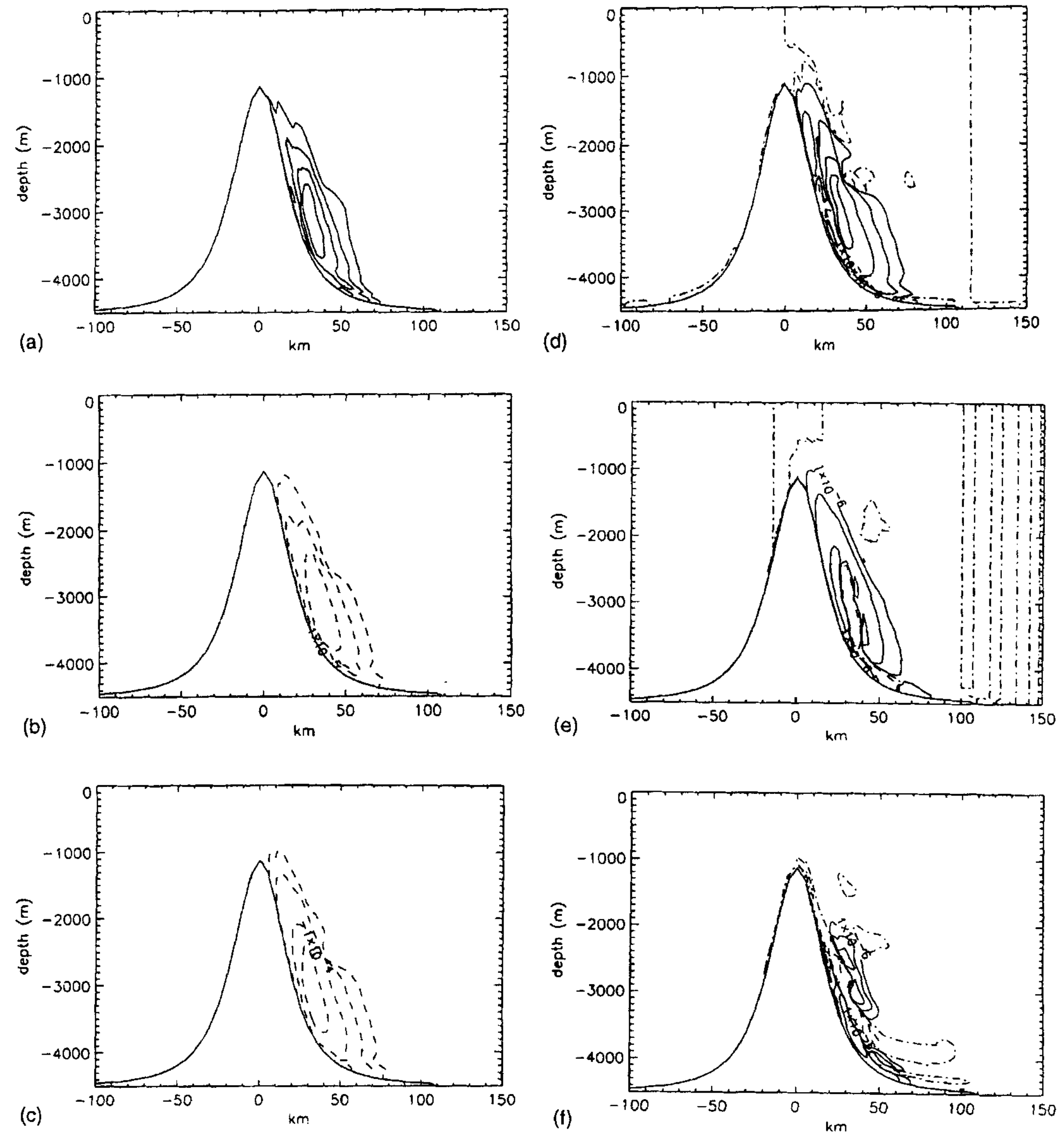

Figure 8. As in Figure 5, but for $\delta = 0{\cdot}75$

The influence of the seamount height on the flow can be further explored by showing the density and flow near the bottom. The important relevant non-dimensional parameter here is the Froude number based on the seamount height, i.e. $F' = U_i/Nh_0$, which is a measure of the non-linearity. Existing theories based on the atmospheric flow over mountains are valid only when $F' \gg 1$ (linear wave theory[7] and $F' \ll 1$ (potential flow theory[39]). Laboratory and numerical methods have been used to study the stratified flow over obstacles outside the range of linear theory and potential flow theory.[38,40–42] Although a detailed study of the small-Froude-number oceanic flow over a seamount is beyond the scope of this paper, the numerical results from three different seamount heights (corresponding to the seamount-height-based Froude numbers 0·67, 0·4 and 0·27) give a flavour of this topic. Figures 9–11 show the density anomaly (defined by the density minus the initial density), relative velocity and flow vectors computed on the lowest model level for different seamount heights. In the case of $\delta = 0{\cdot}3$ ($F' = 0{\cdot}67$, Figure 9) the density anomaly contours basically follow the bottom topography, although there is a small distortion downstream of the seamount centre. In the region downstream of the seamount, internal lee waves are clearly seen from the relative vorticity contours and the flow vectors. Over the seamount the dominant feature is an anticyclonic circulation with a maximum anticyclonic vorticity of about $0{\cdot}7f$, where f is the Coriolis parameter. As the seamount height increases to $\delta = 0{\cdot}5$ ($F' = 0{\cdot}4$), there are dramatic changes in the flow structure (compare Figures 9 and 10). Both positive and negative density anomalies appear over the lee side of the seamount, resulting in a pair of vertically oriented vortices. In a study of the non-rotational atmospheric flow over mountains, Smolarkiewicz and Rotunno[38] found that as the Froude number passed below a critical value (in their case 0·5), vertically oriented vortices on the lee side, with a zone of flow reversal on the windward side, appeared. They explained the mechanism for the generation of the vertically oriented vortices in terms of the tilting of the horizontally oriented vortices which are generated by the baroclinic production as the flow passes the obstacle. The role of the earth's rotation in our cases produces vortices which are highly asymmetric, with dominant anticyclonic vortices (in northern hemisphere), with a maximum anticylonic vorticity of about $1{\cdot}3f$ and a maximum cyclonic vorticity of about $0{\cdot}7f$.

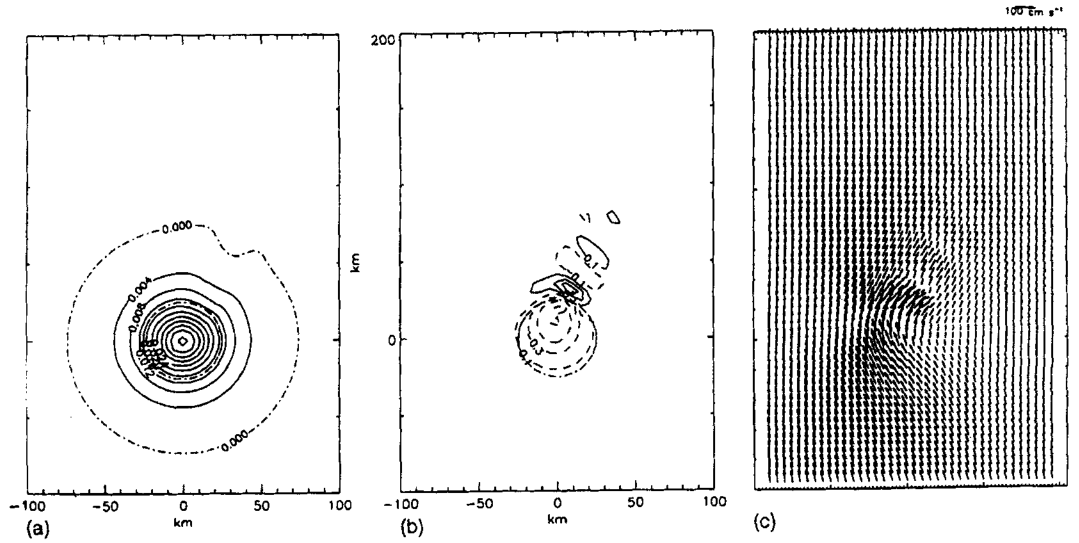

Figure 9. Contours of (a) density anomaly σ_t (kg m^{-3}), (b) relative vorticity (in units of f) and (c) velocity vectors on lowest σ-level computed using a bell-shaped seamount with $\delta = 0{\cdot}3$

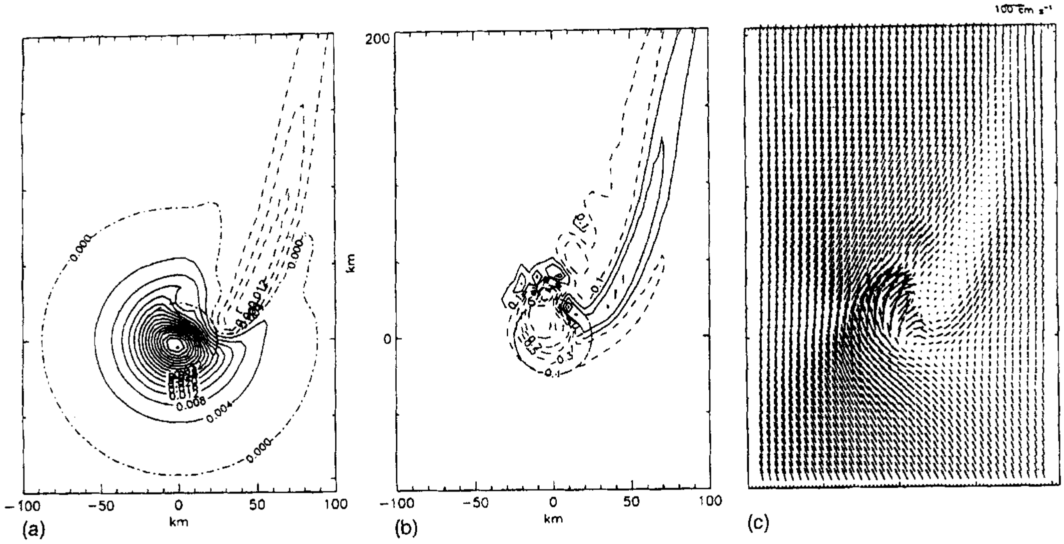

Figure 10. As in Figure 9, but for $\delta = 0{\cdot}5$

These calculations demonstrate qualitatively that the model can accurately represent the non-linear processes necessary to generate the various vortices found in laboratory experiments and other numerical modelling studies.

The case of $\delta = 0{\cdot}75$ ($F' = 0{\cdot}27$) shows further complexity due to the strong non-linearity; in particular, eddy shedding appears (Figure 11). Aspects of eddy shedding have been studied by Boyer and Zhang[43] using laboratory experiments. The fact that the model can accurately represent the eddy-shedding process, together with the passage of the eddy through the northern open boundary without false reflection, provides confidence in the numerical accuracy of the method. The significant spatial

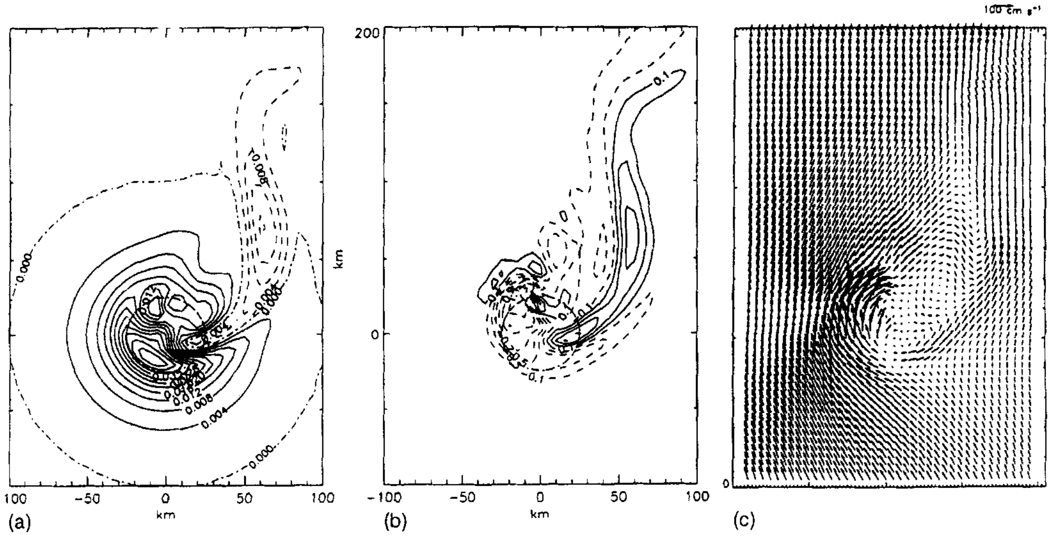

Figure 11. As in Figure 9, but for $\delta = 0{\cdot}75$

variability found in these calculations suggests that a detailed field measurement programme will be required to collect a comprehensive data set for model validation. This problem will be discussed later in the paper.

The bottom friction has a significant influence on the near-bottom flow. Results from a numerical experiment using a free slip bottom boundary condition clearly show a pair of vortices over the lee side of the seamount; in particular, the maximum cyclonic vorticity, being $1{\cdot}5f$, is almost as much as the maximum anticylonic vorticity (Figure 12). This compared with a much smaller cyclonic vorticity over the lee side of the seamount in the case of bottom friction (Figure 10).

This series of calculations has clearly shown that accurate flow fields (in excellent agreement with the CH93 functional/spectral model) can be obtained using the finite difference model with an irregular grid in the vertical. The analysis of the various terms in the turbulence energy model shows that to first order the shear production and turbulence dissipation terms are comparable, although in regions of strong vertical density gradient the suppression of turbulence by stable stratification is particularly important. However, the terms describing the vertical diffusion of turbulence and its advection cannot be neglected, suggesting that a turbulence model in which these terms are omitted may not be universally appropriate and could lead to significant errors depending upon the height of the seamount. In the next subsection we will examine the accuracy of simpler turbulence models by comparison with the solution computed with the full turbulence energy equations.

3.3. Results using the one-equation TKE model and Richardson-number-dependent eddy viscosity

Compared with the two-equation TKE model, the one-equation TKE model is computationally more efficient, although the need to specify the turbulence length scale in the model is a disadvantage. Using the length scale formulation (20) and inequality (17), we repeat the case of $\delta = 0{\cdot}5$. The computed TKE and eddy viscosity are much larger than those determined with the two-

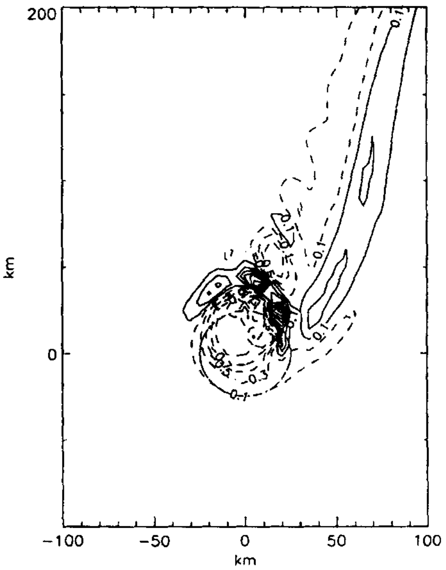

Figure 12. As in Figure 10(b), but without bottom friction (free slip bottom boundary condition)

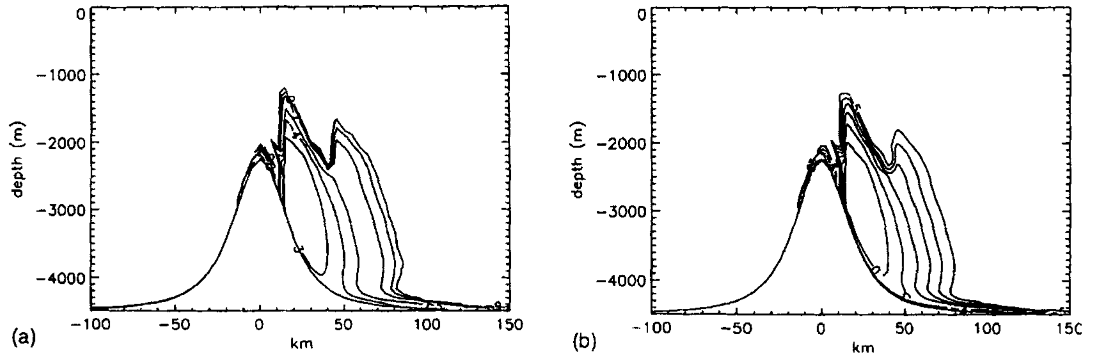

Figure 13. Vertical sections of (a) TKE ($\log_{10}(\mathrm{m}^2\ \mathrm{s}^{-2})$) and (b) vertical eddy viscosity ($\log_{10}(\mathrm{m}^2\ \mathrm{s}^{-1})$) computed using one-equation TKE model. A bell-shaped seamount with $\delta = 0{\cdot}5$ was used in the calculation

equation model (Figures 13 and 14). There is a small change in the internal lee wave amplitude measured by the vertical velocity (not shown here), but the overall wave pattern is similar to the results of the two-equation model.

Apart from different empirical constants in these two TKE closure schemes, one important difference is that the length scale (20) is not influenced by the density stratification in our one-equation model. In the two-equation model used here, the stratification has an influence on both the TKE and the length scale. Furthermore, the eddy viscosity and diffusivity are proportional to stability functions, defined in (15) and (16), which are functions of the buoyancy frequency. It seems that in a stratified flow the length scale should be modified by the stable stratification.[34] As a sensitivity test, we modify the length scale (20) using a similar stability function to that defined in (23); thus the length scale takes the form

$$l_{\mathrm{m}} = l(1 + 10Ri)^{-1/2}, \qquad (41)$$

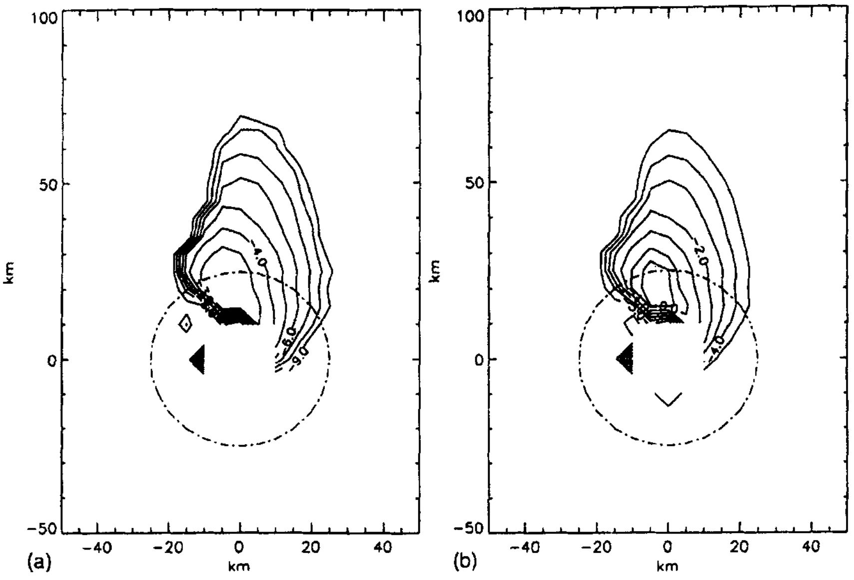

Figure 14. As in Figure 13, but showing horizontal contours at a depth of 2500 m

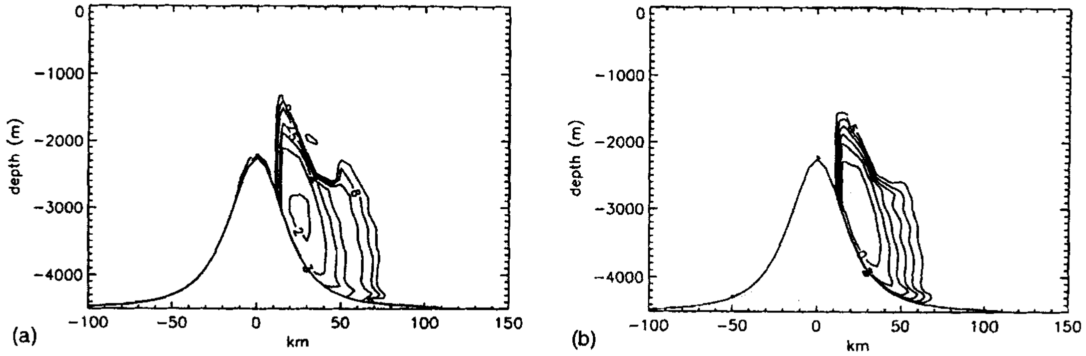

Figure 15. As in Figure 13, but with length scale modified as in (41)

where the Richardson number Ri is defined by (25). The computed TKE and eddy viscosity using the modified length scale are shown in Figures 15 and 16. Compared with the results from the two-equation model shown in Figures 3 and 4, both the TKE and the eddy viscosity are very similar, although the computed eddy viscosity is still larger in the one-equation case.

The method using the Richardson number to compute the eddy viscosity and diffusivity (equations (21) and (22)) is widely applied in both deep sea and coastal oceanography.[44,45] It has major advantages in terms of computational cost and often works very well in some cases. It can in essence be regarded as the lowest order of the turbulence energy balance in a stratified flow. In our application we set $A_{r1} = 0{\cdot}01\ \mathrm{m}^2\ s^{-1}, B_{r1} = 0{\cdot}0001\ \mathrm{m}^2\ s^{-1}, A_{r2} = 0{\cdot}001\ \mathrm{m}^2\ \mathrm{s}^{-1}$ and $B_{r2} = 1{\cdot}4 \times 10^{-6}\ \mathrm{m}^2\ \mathrm{s}^{-1}$ (molecular viscosity) in (21) and (22). The constants given here result in a relatively smaller eddy viscosity and eddy diffusivity compared with the results from the turbulence models. Therefore the internal lee wave amplitude is much larger, with a maximum vertical velocity over $3{\cdot}5\ \mathrm{cm\ s}^{-1}$,

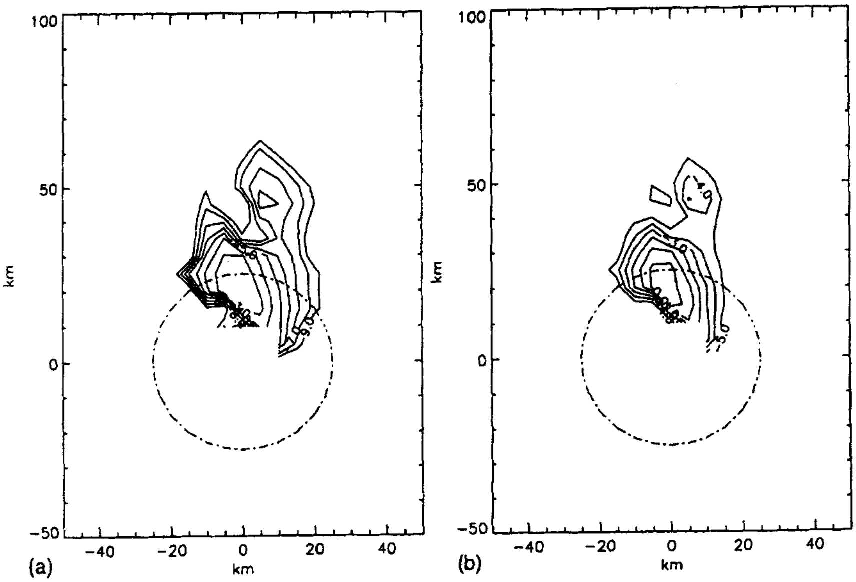

Figure 16. As in Figure 14, but with length scale modified as in (41)

compared with a maximum vertical velocity of about 2·5 cm s^{-1} in the previous cases, although the overall wave pattern changes very little. In Figure 17 we show the vertical sections of Richardson number and computed eddy viscosity taken through the centre of the seamount. It can be seen here that over the lee side of the seamount the Richardson number is very small ($Ri \leqslant 0{\cdot}25$), indicating possible dynamical instability. The $Ri = 0{\cdot}25$ contour roughly corresponds to the 10^{-3} m^2 s^{-2} TKE contour from the results of the turbulence model. The computed eddy viscosity is less than 10^{-2} m^2 s^{-1} even on the lee side. One important feature using the Richardson-number-dependent eddy viscosity and eddy diffusivity is that the eddy diffusivity is in general much smaller than the eddy viscosity, even if we use the same value for A_{r1} and A_{r2}. Figure 18 shows the Richardson number Ri and stability functions ψ_1 and ψ_2 at a depth of 2500 m. In general ψ_2 is a decade smaller than ψ_1. Compared with the turbulence model results, the minimum Ri (and maximum ψ_1 and ψ_2) is not exactly over the area of maximum TKE, but upstream by about 10 km. The reason for this is that the Richardson number takes only the local balance of TKE shear production and density suppression into account (TKE dissipation being proportional TKE). As shown in the budget of the TKE, the advection of the TKE can be significant over the lee side of the seamount and a Richardson number approach cannot take this into account.

This series of calculations has in essence shown that the one-equation turbulence energy model can give similar results to the two-equation model provided that the mixing length is modified by a stability function depending upon the Richardson number and the mixing length is limited in magnitude in a similar way to that used in the two-equation model. This is an interesting result in that this model is computationally less expensive than the two-equation model. It also explains the success of simulations[20,35] using this simpler model.

The fact that the main features of the flow were reproduced by using an algebraic Richardson-number-dependent viscosity and diffusivity goes some way to explaining the success of this type of model, which has mainly been tested by its ability to reproduce large-scale features of the flow. However, its inability to reproduce the mixing features found in the turbulence models can be readily understood in terms of the detailed analysis of the turbulence energy budget performed earlier.

In the calculations considered so far, we have concentrated upon the parametrization of the vertical diffusion term. In the next subsection we briefly examine the effect of horizontal diffusion upon the solution. This is particularly important and complementary to any investigation of the parameterization of vertical diffusion, in that there is little point in using a high-order turbulence method in the vertical with a physically unrealistic, highly diffusive parametrization in the horizontal.

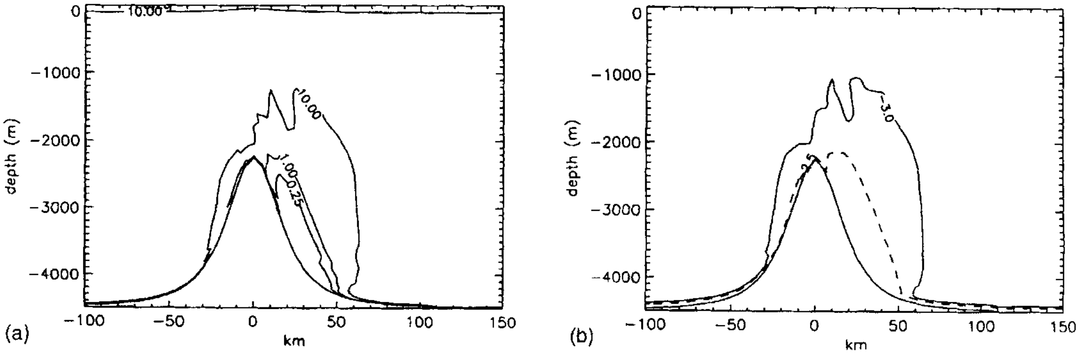

Figure 17. Vertical sections taken through centre of seamount of (a) Richardson number Ri and (b) vertical eddy viscosity ($\log_{10}(m^2\ s^{-1})$) computed using Ri-dependent eddy viscosity formulation

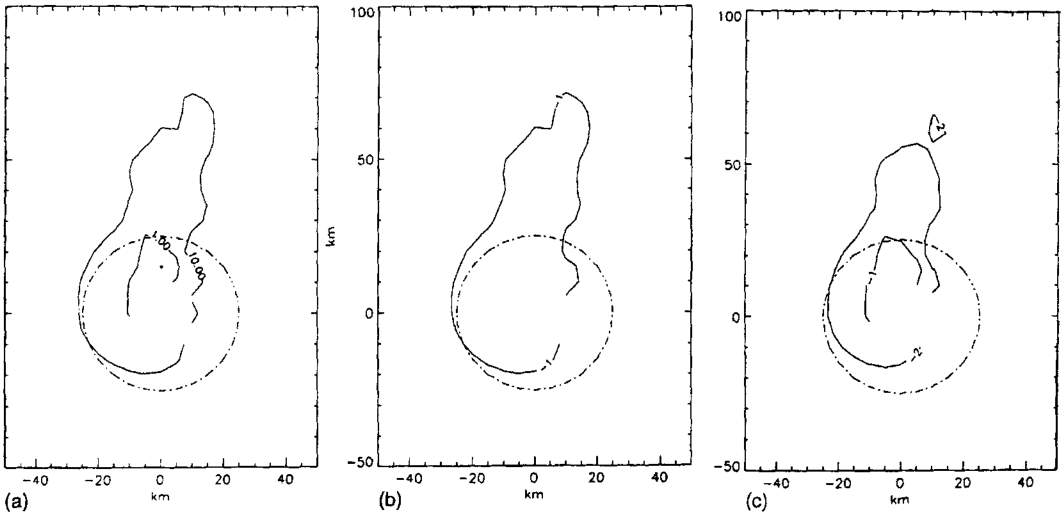

Figure 18. Horizontal distributions of (a) Ri, (b) ψ_1 and (c) ψ_2 at a depth of 2500 m. A bell-shaped seamount with $\delta = 0{\cdot}5$ was used in the calculation

3.4. Sensitivity to the horizontally diffusion formulations

Diffusion in nature is an important phenomenon not only in physical but also in biological and chemical processes. To understand diffusion, it is necessary for us to understand both the transport and mixing processes, an accurate computation of which is important in modelling biological and sedimentation phenomena. Unfortunately, a numerical model has its own complex numerical diffusion associated with the different numerical methods used to solve the equations. The explicit introduction of horizontal diffusion into a model is often for numerical reasons rather than based on physical knowledge. It is known that the different formulations of horizontal diffusion can have significant influences on the computed flow field, in particular in regions of high density gradients. Here two different formulations of horizontal diffusion are used to examine its influence on the solutions.

The previous calculations were all performed using the biharmonic formulation for the horizontal diffusion of momentum and temperature, with $B_M = B_H = 3{\cdot}2 \times 10^9$ m^4 s^{-1}. In order to see the influence of a different formulation of horizontal diffusion, we perform some numerical experiments using the Laplacian form of diffusion. Following Heathershaw *et al.*,[18] in a simple one-dimensional linear case the relation between A_M and B_M is given by

$$\frac{B_M}{A_M} = \frac{(\Delta x/2)^2}{\sin^2[(2\pi/L)\Delta x/2]}, \tag{42}$$

where Δx is the horizontal resolution and L is the wavelength. For the smallest resolvable wavelength, i.e. $L = 2\Delta x$, the same damping for either horizontal diffusion operator is obtained when

$$A_M = \frac{4B_M}{(\Delta x)^2}. \tag{43}$$

With $B_M = 3{\cdot}2 \times 10^9$ m^4 s^{-1} and $\Delta x = 5000$ m (the value used in the present calculation), this yields $A_M = 512$ m^2 s^{-1}.

The results from a numerical experiment with $A_M = 510\ \mathrm{m}^2\ \mathrm{s}^{-1}$, using the two-equation TKE model and $\delta = 0{\cdot}5$, show very strong damping effects on the internal lee waves, with the maximum vertical velocity being halved compared with the case of $B_M = 3{\cdot}2 \times 10^9\ \mathrm{m}^4\ \mathrm{s}^{-1}$. Since the internal lee wave wavelength is of the order of 25 km, we chose $L = 25$ km in (42), which yields $A_M = 180\ \mathrm{m}^2\ \mathrm{s}^{-1}$. The results using $A_M = 180\ \mathrm{m}^2\ \mathrm{s}^{-1}$ and $\delta = 0{\cdot}5$ are shown in Figure 19(a). Compared with the results using biharmonic horizontal diffusion, the stronger damping effect on the internal lee waves, especially further downstream of the seamount, is clearly seen.

Further numerical experiments were performed with a reduction of the coefficients of horizontal diffusion to $B_M = 1{\cdot}6 \times 10^9\ \mathrm{m}^4\ \mathrm{s}^{-1}$ and $A_M = 90\ \mathrm{m}^2\ s^{-1}$. This should have the same damping effect on waves with a wavelength of 25 km. The results using the biharmonic formulation of diffusion show a larger internal lee wave amplitude, especially in the downstream area (Figure 19(b)). The results using the Laplacian formulation of diffusion, however, are very noise (Figure 19(c)). In fact, the damping of the smallest resolvable wavelength ($L = 2\Delta x$) is not sufficient to perform a longer numerical integration. These two examples show the advantages of the biharmonic formulation of horizontal diffusion in problems involving short-wavelength internal waves.

These calculations illustrate the importance of using the more accurate and scale-selective biharmonic form of the horizontal diffusion term if an improved solution is going to be obtained by using a turbulence energy model in the vertical.

Obviously, in physically realistic simulations of oceanographic flows a detailed description of the topography of the seamount is required. In order to understand how accurately the topography must be measured in order to validate turbulence energy models against point measurement made in the vicinity of seamounts, a sensitivity study of the variations in turbulence in response to changes in topography is required. This is performed in the next sub-section.

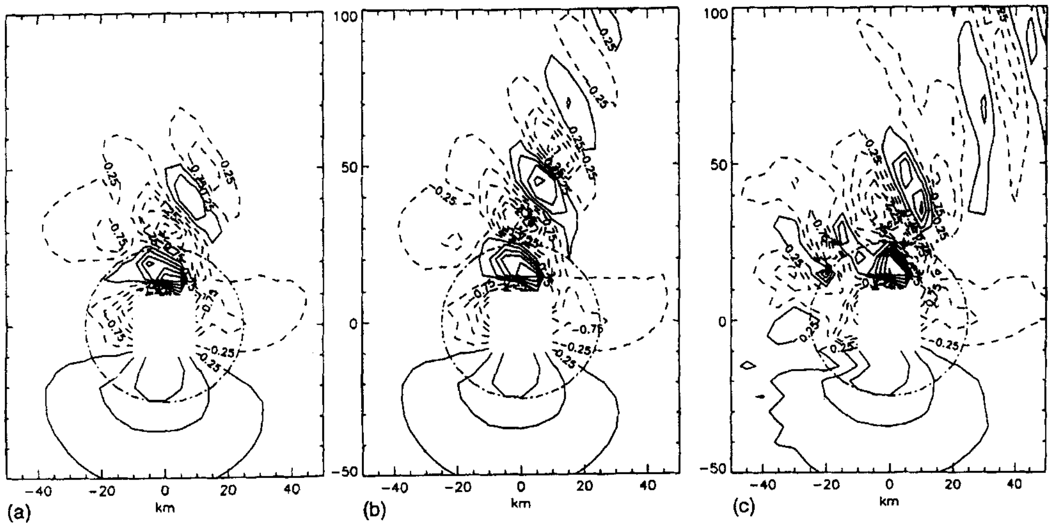

Figure 19. Contours of vertical velocity at a depth of 2500 m computed using (a) Laplacian form of horizontal diffusion, $A_M = A_H = 180\ \mathrm{m}^2\ \mathrm{s}^{-1}$, (b) biharmonic form of horizontal diffusion, $B_M = B_H = 1{\cdot}6 \times 10^9\ \mathrm{m}^4\ \mathrm{s}^{-1}$, (c) as (a) but with $A_H = A_M = 90\ \mathrm{m}^2\ \mathrm{s}^{-1}$. A bell-shaped seamount with $\delta = 0{\cdot}5$ was used in the calculation

3.5. Results using different seamount profiles

All the numerical experiments shown in this paper so far have used a bell-shaped seamount profile. As can be seen in Figure 1, compared with the Gaussian-shaped and cosine-squared seamounts, the bell-shaped seamount has a relatively gentle slope near the sea bed. Using different profiles, we performed further numerical experiments on the flow over an isolated seamount in order to study the sensitivity of the solution to profile changes.

The experiments were performed using the two-equation turbulence model and biharmonic horizontal diffusion with $B_M = B_H = 3{\cdot}2 \times 10^9$ m^4 s^{-1}. Figure 20 shows the vertical sections of vertical velocity, streamwise velocity and vertical eddy viscosity for the Gaussian-shaped and cosine-squared seamounts. Compared with the bell-shaped case in Figure 3, there are three important features. Firstly, the internal lee wave amplitude measured using the maximum vertical velocity

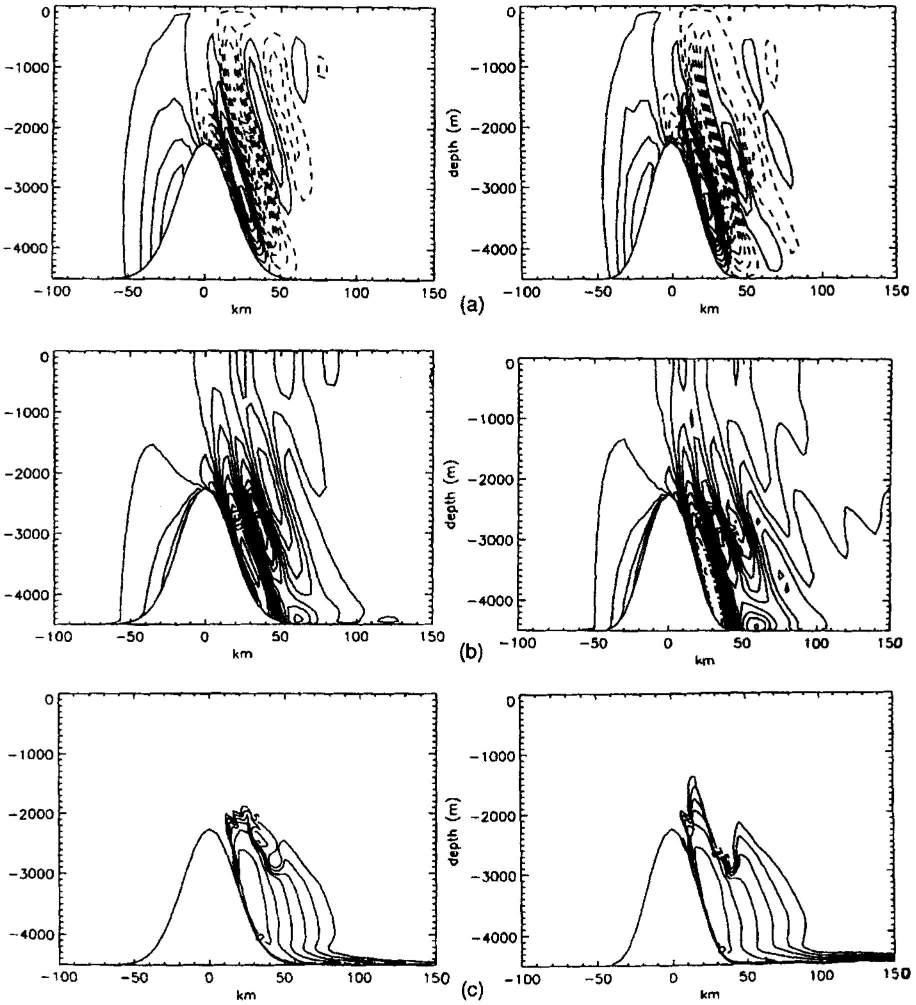

Figure 20. Vertical sections of (a) vertical velocity (contours begin with ±0·25 cm s^{-1} with an interval of 0·5 cm s^{-1}), (b) streamwise velocity (cm s^{-1}) and (c) vertical eddy viscosity ($\log_{10}$(m^2 s^{-1})) taken through seamount centre: left column, Gaussian-shaped seamount; right column, cosine-squared seamount

increases when using the Gaussian-shaped and cosine-squared seamounts. The maximum upwelling velocity over the lee side is about 2·25 cm s^{-1} for the bell-shaped seamount, 2·75 cm s^{-1} for the Gaussian-shaped seamount and 4·35 cm s^{-1} for the cosine-squared seamount. Secondly, flow separation can be seen over the lee side of the cosine-squared seamount in this vertical section, but not for the other two seamount profiles. Thirdly, although the turbulence energy (not shown here) and eddy viscosity are similar over the lee side of the seamount, the TKE and eddy viscosity are larger over the downstream area between $y = 50$ and 100 km. More importantly, near the bottom the TKE and eddy viscosity are much larger for the Gaussian-shaped and cosine-squared seamounts, particularly in the later case.

These calculations suggest that in any detailed study of the flow and mixing in the region of a seamount it will be necessary to accurately determine the geometry and water depth distribution associated with the seamount.

4. CONCLUDING REMARKS

In the first part of this paper we have described the development of a three-dimensional free surface model with a range of turbulence energy submodels for the computation of subgrid-scale mixing. A finite difference grid is used in the vertical to discretize the equations and the accuracy of the solution is established by comparing results with those computed by CH93.[15]

Calculations are performed over a range of seamount heights to examine the effects of height upon the amplitude of the internal lee waves and the magnitude of the resulting turbulence. A range of turbulence energy models from complex to simple is used in these calculations.

The results from the two-equation turbulence model show that the maximum turbulence energy, occurring over the lee side of a seamount upwelling area, can be as much as 10^{-2} m^2 s^{-2}, resulting in strong turbulence mixing. The computed vertical eddy viscosity and eddy diffusivity coefficients have a maximum of about 1 m^2 s^{-1}. Such strong mixing must have important influences on chemical and biological processes and sediment transport. The one-equation turbulence model shows similar results as long as the specified length scale takes account of the influence of the density stratification on the mixing length.

The fact that the one-equation model gives similar results to the two-equation model helps to explain the success of the former model in oceanographic simulations.[20] Also the computational savings associated with this model make it an attractive alternative to the application of the two-equation model.

The turbulence energy budget analysis shows that the main balance terms in the turbulence energy equation are the turbulence shear production, turbulence dissipation and density suppression. However, the advection of the TKE can locally be of a similar order, in particular for a tall seamount. In shallow homogeneous tidal seas Xing and Davies[23] did not find this term to be important. However, in stratified conditions, particularly in deep water, it is necessary to retain this term.

From the turbulence energy budget analysis and the comparison with the $q^2 - q^2 l$ model it is clear that there is some inaccuracy in the mixing computed with the algebraic Richardson-number-dependent parametrization, although the larger-scale features of the flow can be reproduced with this simple parametrization.

Compared with the atmospheric flow over mountains, in which case the earth's rotational effects can often be neglected, the earth's rotation plays a fundamental role in the propagation downstream of internal lee waves. However, there are still some similarities in the bottom flow structure, in particular over the lee side of the mountain, where a pair of vertically oriented vortices can be found in the case of a tall seamount. The earth's rotation results in vortices which are highly asymmetric, with dominate anticyclonic vortices (in the northern hemisphere). Also, bottom friction can modify the bottom vortices significantly. Since the magnitude of the bottom friction depends upon the bed roughness, this suggests that an accurate simulation of the flow in the region of seamounts may require not only detailed measurements of current for model validation but also surveys of bed roughness to ensure its correct representation in the model. Also, the significant spatial variability of the flow and turbulence energy suggests that the limited sets of field data at present collected in the vicinity of seamounts may be inadequate to validate models of flow in these regions. In particular, the calculations using different-shaped seamounts show the importance of an accurate topographic description of these features in order to determine the flow fields and mixing. This also implies that a significant survey of water depths in the region of seamounts is required.

Two different horizontal diffusion formulations are used, namely the biharmonic form and Laplacian form. The results of the experiments show that the biharmonic form of horizontal diffusion has clear advantages in controlling computational noise without imposing unrealistically high damping on the internal lee waves. This suggests that in any large-scale ocean circulation model the biharmonic form of horizontal diffusion is preferable in calculations designed to examine small-scale features.

REFERENCES

1. J. N. Aldrige and A. M. Davies, 'A high-resolution three dimensional hydrodynamic tidal model for the Eastern Irish Sea', *J. Phys. Oceanogr.*, **23**, 207–224 (1993).
2. A. M. Davies and J. N. Aldridge, 'A stable algorithm for bed friction in three dimensional shallow sea modal models', *Int. j. numer. methods fluids*, **14**, 477–493 (1992).
3. R. W. Lardner and S. K. Das, 'Optimal estimation of eddy viscosity for a quasi-three-dimensional numerical tidal and storm surge model', *Int. j. numer. methods fluids*, **18**, 295–312 (1994).
4. S. G. Sajjadi and J. N. Aldridge, 'Prediction of turbulent flow over rough asymmetrical bed forms', *Appl. Math. Model.*, **19**, 139–152 (1995).
5. A. E. Gill, *Atmosphere–Ocean Dynamics*, Academic Press, New York, 1982.
6. B. Gjevik and T. Marthinsen, 'Three-dimensional lee-wave patterns', *Q. J. R. Meteorol. Soc.*, **104**, 947–957 (1978).
7. R. B. Smith, 'The influence of mountains on the atmosphere', *Adv. Geophys.*, **21**, 87–230 (1979).
8. R. B. Smith, 'Hydrostatic air flow over mountains', *Adv. Geophys.*, **31**, 1–41 (1989).
9. P. G. Baines 'On internal tide generation models', *Deep-Sea Res.*, **29**, 307–338 (1982).
10. P. D. Craig, 'Solution for internal tidal generation over coastal topography', *J. Marine Res.*, **45**, 59–76 (1987).
11. A. L. New, 'Internal tidal mixing in the Bay of Biscay', *Deep-Sea Res.*, **35**, 691–709 (1988).
12. T. J. Sherwin and N. Taylor, 'Numerical investigations of linear internal tide generation in the Rockall Trough', *Deep-Sea Res.*, **37**, 1595–1618 (1989).
13. J. M. Huthnance, 'Internal tides and waves near the continential shelf edge', *Geophys. Astrophys. Fluid Dyn.*, **48**, 81–106 (1989).
14. J. M. Huthnance, 'Circulation, exchange and water masses at the ocean margin: the role of physical processes at the shelf edge', *Prog. Oceanogr.* **35**, 353–431 (1995).
15. D. C. Chapman and D. B. Haidvogel. 'Generation of internal lee waves trapped over a tall isolated seamount', *Geophys. Astrophy Fluid Dyn.*, **69**, 33–54 (1993).
16. W. G. Large, J. C. McWilliams and S. C. Dorey, 'Oceanic vertical mixing: a review and a model with nonlocal boundary layer parameterization', *Rev. Geophys.*, **32**, 363–403 (1994).
17. W. R. Crawford, 'Tidal mixing and nutrient flux in the waters of southwest British Columbia', B. B. Parker (ed.), *Tidal Hydrodynamics*, Wiley, New York, 1991, pp. 855–872.
18. A. D. Heathershaw, J. Small and C. E. Stretch, 'Frictional formulations in numerical ocean models and their effect on simulated acoustic fields', *J. Phys. Oceanogr.*, **24**, 274–297 (1994).
19. G. L. Mellor and T. Yamada 'Development of a turbulence closure model for geophysical fluid problem', *Rev. Geophys. Space Phys.*, **20**, 851–875 (1982).
20. B. Johns and T. Oguz, 'Turbulence energy schemes', in N. S. Heaps (ed.), *Three-Dimensional Coastal Ocean Models*, American Geophysical Union, 1987, pp. 17–40.
21. W. H. Munk and E. R. Anderson, 'A note on the theory of thermocline', *J. Marine Res.*, **26**, 276–285 (1948).
22. A. M. Davies and J. E. Jones, 'Application of a three-dimensional turbulence energy model to the determination of tidal currents on the northwest European shelf', *J. Geophys. Res.*, **95**, 18, 143–18, 162 (1990).
23. J. Xing and A. M. Davies, 'Application of three dimensional turbulence energy model to the determination of tidal mixing and currents in a shallow water', *Prog. Oceanogr.*, **35**, 153–205 (1995).

24. J. Xing and A. M. Davies, 'Application of a range of turbulence energy models to the determination of M_4 tidal current profiles', *Continental Shelf Res.*, **16**, 517–547 (1996).
25. A. M. Davies and J. Xing 'An intercomparison and validation of a range of turbulence closure schemes used in three dimensional tidal models', in D. R. Lynch and A. M. Davies (eds), *Quantitative Skill Assessment for Coastal Ocean Models*, American Geophysical Union, Washington, 1995, pp. 71–95.
26. G. L. Mellor and T. Yamada 'A hierarchy of turbulence closure models for planetary boundary layers', *J. Atmos. Sci.*, **31**, 1791–1806 (1974).
27. A. F. Blumberg and G. L. Mellor, 'A description of a three-dimensional coastal ocean circulation model', in N. S. Heaps (ed.), *Three-Dimensional Coastal Ocean Models*, American Geophysical Union, Washington, 1987, pp. 1–16.
28. L. -Y. Oey and P. Chen, 'A model simulation of circulation in the Northeast Atlantic shelves and seas', *J. Geophys. Res.*, **97**, 20,087–20, 115 (1992).
29. J. Xing and A. M. Davies, 'The influence of mixing length formulation and stratification upon tidal currents in shallow seas', *Estuar. Coastal Shelf Sci.*, **42**, 417–456.
30. B. Galperin, L. H. Kantha, S. Hassid and A. Rosati, 'A quasi-equilibrium turbulent energy model for geophysical flows', *J. Atmos. Sci.*, **45**, 55–62 (1988).
31. B. Galperin, A. Rosati, L. H. Kantha and G. L. Mellor, 'Modeling rotating stratified turbulent flows with appliction to oceanic mixing layers', *J. Phys. Oceanogr.*, **19**, 901–916 (1989).
32. Z. I. Janjic, 'The step-mountain coordinate: physical package', *Mon. Weather Rev.*, **118**, 1429–1443 (1990).
33. J. P. Gerrity and T. L. Black, 'The numerical solution of the Mellors–Yamada level 2·5 turbulent kinetic energy equation in the eta model', *Mon. Weather Rev.*, **112**, 1640–1646 (1994).
34. P. J. Luyten, 'An analytical and numerical study of surface and bottom boundary layers with variable forcing and application to the North Sea', *J. Marine Syst.*, in press.
35. B. Johns and J. Xing, 'Three-dimensional modelling of the free-surface turbulent flow of water over a bed form', *Continental Shelf Res.*, **13**, 705–723 (1993).
36. D. C. Chapman and D. B. Haidvogel, 'Formation of Taylor caps over a tall isolated seamount in a stratified ocean', *Geophys. Astrophy. Fluid Dyn.*, **64**, 31–65 (1992).
37. Y. Song and D. B. Haidvogel, 'A semi-implicit ocean circulation model using a generalized topography-following coordinate system', *J. Comput. Phys.*, **115**, 228–244 (1994).
38. P. K. Smolarkiewicz and R. Rotunno, 'Low-Froude number flow past three-dimensional obstacles. Part I: Baroclinically generated lee vortices', *J. Atmost. Sci.*, **46**, 1154–1164 (1989).
39. P. G. Drazin, 'On the steady flow of a fluid of variable density past an obstacle', *Tellus*, **13**, 239–251 (1961).
40. C. R. Hunt and W. H. Snyder, 'Experiments on stably and neutrally stratified flow over a model three-dimensional hill', *J Fluid Mech.*, **96**, 671–704 (1980).
41. D. L. Boyer, P. A. Davies, W. R. Holland, F. Biolley and H. Honji, 'Stratified rotating flow over and around isolated three-dimensional topography', *Philos. Trans. R. Soc. Lond. A*, **322**, 213–241 (1987).
42. P. M. A. Miranda and I. N. James, 'Non-linear three-dimensional effects on gravity-wave drag: splitting flow and breaking waves', *Q. J. R. Meteorol. Soc.*, **118**, 1057–1081 (1992).
43. D. L. Boyer and X. Zhang, 'Motion of oscillatory currents past isolated topography', *J. Phys. Oceanogr.*, **20**, 1425–1448 (1990).
44. A. E. Gargett, 'Parameterizing the effects of small-scale mixing in large-scale numerical models', in *NATO ASI Ser. 1: Global Environmental Change*, Vol. II, Modelling Oceanic Climate Interactions, Springer-Verlag, Berlin, 1993, 185–204.
45. I. D. James, 'A primitive equation model simulation of eddies in the Norwegian coast current', *J. Phys. Oceanogr.*, **21**, 893–902 (1991).